

Simulation-based characterization of electrolyte and small molecule diffusion in oriented mesoporous silica thin films

Bin Sun^{1*}, Ryan Blood^{1*}, Selcuk Atalay^{1,2+}, Dylan Colli¹, Stephen
E. Rankin³, Barbara L. Knutson³, Peter M. Kekenos-Huskey¹⁺¹

¹Department of Chemistry, University of Kentucky, Lexington,
KY, USA 40506

²Maxwell Institute for Mathematical Sciences, Heriot-Watt
University, Edinburgh, UK EH14 4AS

³Department of Chemical and Materials Engineering, University of
Kentucky, Lexington, KY, USA 40506

October 23, 2017

* contributed equally; + corresponding author

1 Abstract

Mesoporous silica films offer exciting potential for the delivery of molecular cargo, detection of molecular agents and as environment-dependent 'nano reactors' in biological systems. Fundamentally important to realizing this potential are quantitative models for how the material topology, surface chemistry and surface/solution interface govern molecular transport (via diffusion). Partial differential equation (PDE)-based approaches are particularly well-suited for reaction-diffusion processes in materials, given the ability to incorporate into the simulation important details including material morphology, surface chemistry and charge. However, two challenges that hinder the application of reaction-diffusion partial differential equation (PDE)s to structurally-realistic models of materials are 1) burdensome post-processing and annotation of microscopy data needed for PDE solutions and 2) challenges in extrapolating model predictions determined at the nanoscale to heterogeneous materials. To address this gap, we developed a new workflow for simulating ion reaction-adsorption-diffusion in nanoporous silica-based materials that are resolved through electron microscopy. Firstly, we propose a matched filtering procedure to identify and segment unique porous regions of the material that will be subject to PDE simulation. Secondly, we perform reaction-adsorption-diffusion PDE simulations on representative material regions that are then applied to characterize the entire microscopy-resolved film surface. Using this model, we examine the capacity of a recently synthesized mesoporous film to tune small molecule permeation through modulating the material permeability, surface chemistry including buffering and adsorption, as well as electrolyte composition. Specifically, we find that our proposed matched filtering approach reliably discriminates hexagonal close packed (HCP) porous regions (bulk) from characterized defect regions in transmission electron microscopy (EM) data for nanoporous silica films. Further, based on our implementation of a pH-/surface-chemistry dependent Poisson-Nernst-Planck (PNP) model that is consistent with existing experimental measurements of KCl and CaCl₂ conductance, we characterize ion and 5(6)-Carboxyfluorescein (CF) dye permeability in silica-based nanoporous materials over a broad range of ionic strengths, pHs, and surface chemistries. Using this protocol, we probe conditions for selectively tuning small molecule permeability based on mesoporous film pore size, surface charge, ionic strength and surface reactions in the rapid-equilibrium limit. Altogether, this framework provides means to utilize and validate high resolution microscopy data of mesoporous materials, from which spatially heterogeneous transport parameters can be estimated. As such, the protocol will have significance for characterization of new materials for wide ranging applications.

2 Introduction

2.1 Ion transport in mesoporous films and the impact of defects

Mesoporous silica films have garnered considerable interest for applications to separation chemistry, drug delivery, and biosensors¹⁻⁴ owing to their tunable control of ion mass transport processes within their highly-charged porous networks. In part, this precise tuning is afforded through the high density of silanol groups on silica surfaces,⁵ which can support pH-dependent charge regulation and substrate adsorption in aqueous media.^{6,7} In turn, these surface chemistry phenomena have been shown to modulate ion permeation and con-

ductance, beyond estimations based on restricted diffusion or tortuosity alone. Here electrostatic interactions play a profound role in modulating ion transport, for which the ionic-strength determined electric double layer length scales are on the same order as pore diameters. As a result, there is a rich set of physical phenomena that can emerge in these materials. For instance, two extremes in background ionic strength give insight into the complex tug and pull governing ion transport. At low ionic strengths, potentials arising from surface charges can extend significantly into the bulk fluid phase, where they strongly dictate rates of electrodiffusion. At high ionic strengths, surface potentials are largely attenuated, in which case transport is largely controlled by concentration gradients and differences in osmotic pressure.^{8–10} These phenomena have been characterized in nanoporous 'slits' and 'channels', but have been less explored in nanoporous films with uniform ordered mesopores generated by liquid hexagonal close packed (HCP) (mesocrystalline) templating.^{6,11–14}

Diffusion-limited transport of small molecules in nanoscale media is sensitive to material morphology, surface charges, the solution ionic strength and physiochemical properties of the diffuser such as size and charge. Therefore, a prominent challenge in assessing transport in mesoporous silica films is how these contributions collectively control ion diffusion rates in perfectly-formed porous regions, and the extent to which structural defects perturb these rates. Among these, framework defects are among the most poorly understood factors and are known to perturb substrate diffusivity and permeation in nanoscopic materials.¹⁵ Framework defects in HCP (mesocrystalline) materials share many similarities with mesoporous films, and are categorized by their size as micro ($<20\text{\AA}$), macro ($>500\text{\AA}$), and meso (intermediate),¹⁶ which include cracks and holes representing the predominant macro-scale defects,¹⁶ while imperfect mesoHCP (mesocrystalline) formation or intergrowth account for the majority of meso- and micro-scale defects.¹⁷ Below 500\AA , the most common structural defects include HCP (mesocrystalline) stacking faults resulting in merged pores,^{18,19} inter-growth of different mesoHCP (mesocrystalline) forms^{20,21} and hydroxyl (OH)-terminated surfaces²² (silanol nests). Thus, critical for evaluating and optimizing chemical processes in real materials is a fundamental understanding of mass transport^{22–24} in both ordered (HCP (mesocrystalline)) and defect-containing mesophases.

2.2 Techniques for incorporating microscopy data into nanoscale simulations

Transmission and scanning electron microscopy have become the standard imaging modalities for probing the structural integrity of nanoporous media.^{25,26} Though considerable effort has been invested in characterizing prominent HCP (mesocrystalline) defects in electron micrographs, less has been done to simulate the impact of representative defects on material transport and performance properties. For instance, studies examining gas/liquid adsorption in nanoporous silica with morphological defects have been reported based on molecular simulations,^{27,28} but these were not explicitly linked macroscale transport phenomena. It is our speculation that the abundance of defects and difficulty in translating these structural features to forms amenable to simulations have challenged probing via simulation nanoscale transport phenomena in structurally-imperfect nanoporous media. Here, advances in automated segmentation of electron microscopy data has the potential to ease the burden of manual identification and characterization of material structural features, which could serve as the basis for detailed substrate transport simulations. Recent examples include utiliz-

ing image processing such as equalization, segmentation and Shannon entropy to characterize porosity and other features in nanomaterials.^{29–32} Conversely, techniques for reconstructing 3D structures from 2D EM slices are widely implemented for investigating nanoparticle and nanocatalyst structures in complex hierarchical arrangements.^{33,34}

2.3 Modeling approaches for ionic transport in mesoporous media

Computational models for estimating the extent to which defects impact nanoporous material performance could improve material design, yet most approaches assume perfectly ordered mesoporous materials. For perfect (defect-free) nanoporous silica materials, a variety of simulation approaches have been developed to characterize substrate adsorption and transport, including continuum, stochastic methods such as Monte Carlo and molecular dynamics simulations (reviewed in³⁵). While molecular simulations provide a powerful toolset for probing atomic-level physical phenomena including local self-diffusion, hydration and adsorption,^{36–38} continuum transport simulations constitute a multi-scale complement to extrapolate nanoscale molecular-scale physiochemical information to macroscopic phenomena occurring in nanoporous material.^{39–41} Among the most successful models of ion transport at the continuum level is Poisson-Nernst-Planck (PNP) theory, which is a continuum model of electrostatically-driven ion diffusion coupled with ion-dependent electrostatic fields. Recent developments have augmented Poisson-Nernst-Planck (PNP) simulations to include pH-regulated surface charge⁴¹ for modeling ion conductance in nanoporous materials. Despite the wealth of simulation effort targeting nanoscale materials, how ionic transport might vary in heterogeneous or defect-containing nanoporous materials is under explored.

2.4 Paper Objectives

In this study, we have developed a workflow as a foundational step toward imaging-informed, computational modeling of ion transport in mesoporous silica films with structural defects. This workflow (Fig. 1) enlists a computer vision technique, matched filtering, to 1) discriminate HCP from defect-containing regions from EM 2) performs partial differential equation simulations of electrokinetic transport in 3D models of such regions, and 3) estimates heterogeneous effective transport parameters in a given material. Step 1 utilizes matched filtering to automatically detect mesocrystalline features for EM. In this procedure, kernels representing such features are convolved against the data; the kernel generating the maximal response above a user-defined signal-to-noise ratio is used to annotate the region in the data. Step 2 the kernels developed for step 1 are converted into 3D meshes by projecting the 2D signature perpendicular to plane to create a 3D pore. Step 3 A pH- and surface charge-dependent model of electrolyte transport (PNP) partial differential equation is solved in the 3D meshes using the finite element method, from which effective transport parameters such as conductivity and diffusion are calculated. Step 4 is to interpolate the effective parameters from Step 3 onto the annotated regions determined in Step 1. We applied this to a mesoporous silica film synthesized and characterized by Wooten et al⁴² (electron microscopy data in Fig. 3) as well as simulated data to demonstrate the algorithm performance.

We demonstrate that our workflow for the first time automates electrokinetic transport simulations in microscopy-derived, defect containing structural

data of mesoporous films. Our proposed computer vision method demonstrates reasonable accuracy in discriminating mesocrystalline (bulk) from defect regions in transmission electron microscopy data and simulated data, thereby providing means to characterize the nature and prevalence of defects. Further, our implementation of the pH-/surface-chemistry dependent PNP model is consistent with experimental measurements of KCl and CaCl₂ conductance in silica-based nanochannels over a broad range of ionic strengths and pHs, delineating regimes that permit simplified electrokinetic models. Without any additional fitting, the model predicts permeation properties of an anionic dye CF in a mesoporous film within experimental uncertainty. With this model, we predict the degree to which defects in a mesoporous film influence permeation properties, the optimal conditions under which to make these variations apparent, and conditions for selectively tuning small molecule permeability based on pore size, charge and buffering. Overall, we envision that this model will provide rigorous means to characterize high resolution microscopy data, from which heterogeneous transport parameters can be estimated. Further, its basis as a finite element model should permit its extension to wide-ranging material types, including hierarchically-structured composite materials.

3 Methods

Our workflow for segmentation and PDE-based simulations of ion transport in EM-resolved nanoporous media is shown in Fig. 1. Key stages of this workflow include 1) automated unit cell feature detection in EM-characterized nanoporous media (Sect. 3.1), 2) three-dimensional meshes based on the detected unit cells (Sect. 3.2), 3) effective transport parameter estimation based on Poisson-Nernst-Planck (PNP) simulations of ion transport within porous regions of each unit cell (Sect. 3.3) 4) extrapolation of unit cell transport parameter estimates onto the imaged material surface (Sect. 3.4).

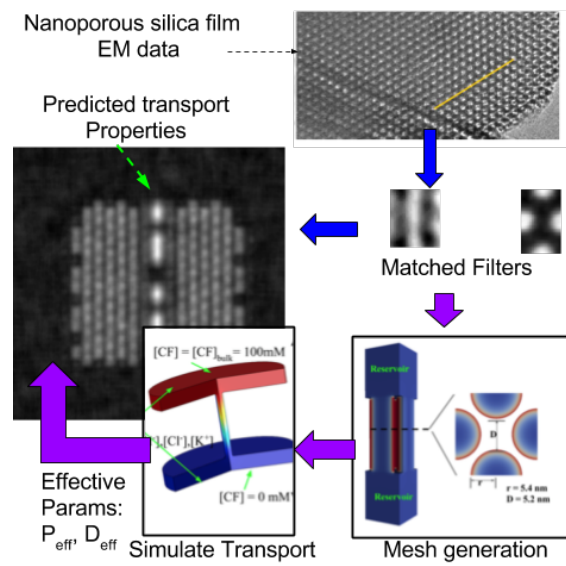


Figure 1: Workflow based on structural data from Wooten et al.:⁴² 1) Matched filter unit cell detection from EM data. 2) 3D geometries construction with meshing. 3) PNP solved in representative unit cell geometries. 4) Interpolate effective transport parameters for entire film from unit cells.

3.1 Matched filter unit cell determination from segmentation of bulk mesocrystal and defect EM data

We utilize 'matched filtering' for the first stage of our workflow, in order to assess the likelihood of a kernel representing a feature of interest is present in a given data set. Consider a measurement, \vec{m} , that consists of a signal, \vec{s} , embedded in additive noise, \vec{n} :

$$\vec{m} = \vec{s} + \vec{n}, \quad (1)$$

The goal of matched filtering is to identify a matched filter, \vec{h} , that maximizes the signal-to-noise ratio (SNR) for a measurement, \vec{m} ,⁴³

$$y = \vec{h}^T \vec{m} = \vec{h}^T \vec{s} + \vec{h}^T \vec{n}, \quad (2)$$

where \vec{h}^T denotes the filter's transpose. It can be shown that the optimal matched filter can be determined via

$$\vec{h} = \frac{1}{\sqrt{\vec{s}^T R_n^{-1} \vec{s}}} R_n^{-1} \vec{s}, \quad (3)$$

where $R_n = E\{nn^T\}$ represents the noise covariance matrix. In the event that random variates are drawn from a mean-zero, Gaussian, white noise process of variance, σ^2 , the noise covariance matrix reduces to $R_n = \sigma^2 \mathbf{I}$, where \mathbf{I} is the identity matrix. Commonly, the signal or multiple instances thereof may be embedded within a larger data set (r), such as an image. In which case, determining the location of s within r is commonly performed by convolving the kernel h with the image, r

$$Y = h * r, \quad (4)$$

Computationally, this is commonly done via the discrete Fourier transform, given that

$$h * r = \mathcal{F}^{-1} [\mathcal{F}[h] \cdot \mathcal{F}[r]], \quad (5)$$

by the convolution theorem. Probable detections of the signal s within Y are based on identifying positions, at which the SNR is above a user-specified threshold criterion, λ ,

$$\text{SNR} \equiv \frac{|\vec{h}^T \vec{s}|}{\vec{h}^T \sigma^2 \mathbf{I} \vec{h}} \geq \lambda, \quad (6)$$

where σ_n represents the standard deviation of the noise.

In this study, we consider a 90nm thick mesoporous silica film with hexagonally-packed, 5nm radius pores (see Fig. 2a) synthesized by Wooten et al,⁴² from which the matched filters were determined. A representative transmission electron microscopy (TEM) image of the film is provided in Fig. S2, which was collected at 68,000x magnification. These data reveal a preponderance of ordered hexagonally-packed pore regions with a small number of defects evident as small linear features. It is speculated that the linear features represent pores that became fused during the film preparation, thereby yielding a 'channel-like' fused pore shown in Fig. 2b. Since the primary goal of the matched filtering is to discriminate bulk regions from defect features, the underlying structure corresponding to the linear feature in the EM is of little significance. Therefore, here we determine the matched filter kernels, or 'filters', based manually identifying representative bulk and 'fused pore' regions in the EM data. We first applied the PYTHON OPENCV 'Contrast Limited Adaptive Histogram Equalization' routine to equalize the pixel intensities across the image. After which,

the identified regions were subdivided into unit cells representing an instance of the nanoporous feature. These subdivisions were averaged to attenuate uncorrelated background noise and reveal the consensus structures shown in Fig. 2, which served as matched filters for each data feature. In our approach, we consider multiple filters that represent different features in the EM data, as well as rotations thereof in order to detect alternate orientations. Since the orientation of the bulk hexagonally-packed regions and fused pore features vary across the EM field of view, we created a bank of filter rotations for each matched filter that were spaced at 10 degree increments. The correlation response for a given image pixel, y_{ij} , was determined by taking the maximum response across all rotated variants of a given filter. Given that the data considered in this study contains signal (nanopores), noise that is not necessarily additive, and other features in the EM data that are not represented by a given filter, h , we modified our threshold criterion as follows

$$\log \frac{\exp(\vec{h}_i^T \vec{s})}{\sigma^2 \gamma \exp(\vec{h}_{iC}^T \vec{s})} \geq \lambda_i, \quad (7)$$

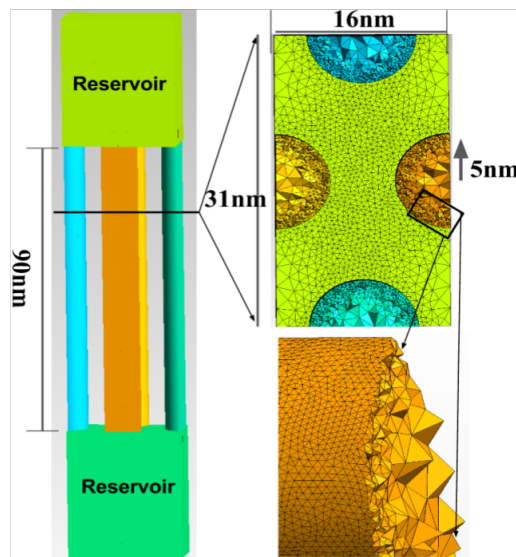
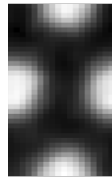
where \vec{h}_{iC} represents the complement of matched filter i , \vec{h}_i , which we define as $\vec{h}_{iC} = 1 - \vec{h}_i$. This complement penalizes signal that falls outside of the signal signature defined in \vec{h}_i . We found this term was necessary to discriminate the correlation outputs from the bulk and fused pore matched filters. We tested both filters against two subsections of Fig. S2, a 'fused pore-rich' region and a 'bulk-like' region (see bottom left panels of Fig. 3 and Fig. S3, respectively). Regions of the test EM data that returned responses below the threshold parameters for either filter are designated as 'uncharacterized.' Details for selecting optimal threshold parameters and corresponding receiver operator characteristic (ROC) curves are provided in Sect. S.2.1. All aforementioned numerical procedures were conducting using the PYTHON2.7 libraries NUMPY, SCIPY and OPENCV-PYTHON.

3.2 Mesh generation from matched filter unit cells

Effective parameter estimation in the second stage of Fig. 1 is based on numerical solution of the PNP equation via the finite element method in Sect. 3.3, using 3D meshes informed from the segmented images. Unit cells determined from our segmentation protocol provided a basis for generation of tetrahedralized, finite element meshes via GMSH,⁴⁴ for which the pore radii and spacings were approximated from the segmented data. In principle, however, the segmented data could be used directly for mesh generation.⁴⁵ From these data, we created 'extruded' unit cells of length 90nm, which assumed the inner pores are perpendicular to the EM-resolved film surface (Fig. 2). The MathEval and Box field in GMSH were used for mesh refinement which ensures finer mesh near nanopore walls. The extruded pores interfaced with two identical reservoirs to represent contact with bulk solution. In principle, the reservoir size should be significantly larger than the pore dimensions to minimize artifacts introduced by the reservoir boundaries on the electrostatic potential adjacent to the silica surfaces.^{46,47} In a recent study,⁴⁸ it was demonstrated that more modestly sized reservoirs on the order of 20 nm were sufficient to minimize these artifacts; here, we set the reservoir depth(z direction) to be 40nm, while the width and length of reservoir are shown as in Fig. 2. Meshes resembling 'nanochannel' and 'nanoslit' geometries were constructed in a similar fashion for the validations described in this study (see Fig. S4). Moreover, we evaluate the conductivities near the midpoint of the silica pores, which is expected to further reduce boundary arti-

facts. In the Results section, we demonstrate good agreement with experimental conductivity measurements, which suggests our choices of domain configuration and conductance measurements (see Methods) were appropriate.

A) Hexagonal(Bulk) Unit Cell



B) Fused pore Unit Cell

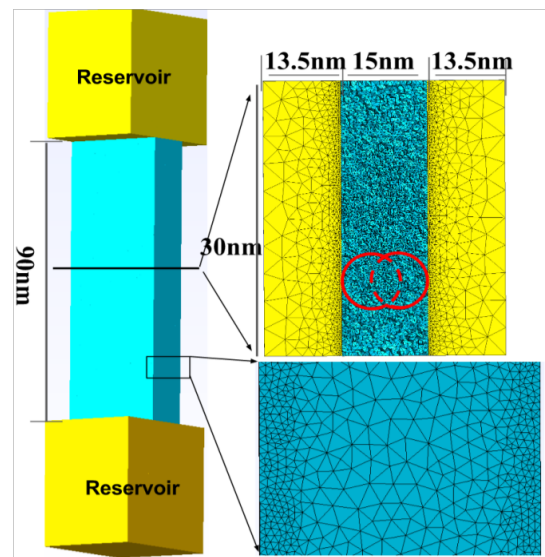


Figure 2: Two unit cells detected by our "matched filter" method based on the EM image of silica membrane fabricated by Wooten et al.⁴² The dimensions of the unit cells were automatically determined by the segmentation procedure. The corresponding 3D geometries (with meshing) generated by GMSH⁴⁴ are also shown. A) Hexagonal(bulk) unit cell. B) Fused pore unit cell.

3.3 Effective transport parameter determination via finite element solutions of the Poisson-Nernst-Planck transport model

The mass transport of ions in a silica nanopore was described by the Poisson-Nernst-Planck (PNP) equation. The Nernst-Planck (NP) equation describes the ionic mass flux density of each ion species subject to concentration and electric potential gradient. Meanwhile, the electric potential distribution within the domain is determined by Poisson equation. These two equations are given as:

$$-\nabla \cdot \mathbf{J}_i = 0, \quad (8)$$

$$\mathbf{J}_i = -D_i \left(\nabla c_i + \frac{z_i F c_i}{RT} \nabla \phi \right), \quad (9)$$

$$-\epsilon_r \epsilon_0 \nabla^2 \phi = F \sum_{i=1}^N z_i c_i, \quad (10)$$

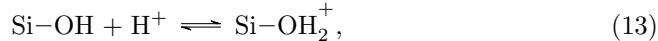
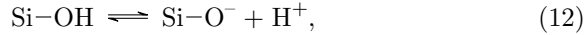
Here, J_i , D_i , c_i , z_i are flux density, diffusion coefficient, molar concentration, and valence electron number of i^{th} ionic species. F is the Faraday constant, ϕ is electric potential, T is absolute temperature, and R is gas constant. ϵ_0 and ϵ_r are vacuum permittivity and the relative permittivity of the electrolyte solution, respectively. The boundary conditions are given as: 1) When evaluating ionic conductance: at the both ends of the reservoir, ionic concentrations are maintained at the bulk values (i.e., $c_i = c_{i,bulk}$) while potentials of $\phi = 0$ and $\phi = 0.2V$ are applied. 2) When evaluating effective diffusion constant/permeability: at the both ends of the reservoir, electric potentials are set as 0 (i.e., $\phi = 0V$) while concentrations of $c_i = c_{i,bulk}$ and $c_i = 0$ are applied at either end. 3) Within the nanopore, we apply a reflective boundary condition for the ions ($\mathbf{n} \cdot \mathbf{J}_i = 0$). 4) A Neumann condition on the potential is also applied based on the silica surface charge density:

$$-\nabla \phi \cdot \mathbf{n} = \sigma_s / (\epsilon_0 \epsilon_r), \quad (11)$$

\mathbf{n} is the unit outer normal vector.

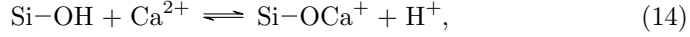
3.3.1 Surface protonation and K^+/Ca^{2+} surface adsorption

Recently, the Qian group and their collaborators have conducted a series of numerical electrodiffusion simulations based on silica nanochannel geometries.^{6,13,49} These models assumed four ionic species, H^+ , OH^- , Cl^- and K^+ , as well as silanol (SiOH) protonation:



The inclusion of the pH-dependent regulation of surface charge density in the PNP model was found to give superior agreement with experimental measurements of KCl conduction at non-neutral pH. More importantly, their results indirectly demonstrate that metal adsorption between the monovalent cations (e.g., K^+) and the channel wall silanol groups is negligible,^{50,51} as their PNP model was sufficient to recapitulate experimental results without considering K^+ adsorption. For divalent cations such as Ca^{2+} , adsorption onto the silica

surface is believed to be significant.^{50,52,53} This motivated a site-binding model for divalent cation adsorption that appeared most consistent with experimental data among several reaction possibilities.⁵⁰



The corresponding equilibrium constants of the (de)protonation and Ca^{2+} adsorption reactions are thus given by

$$K_{a1} = \frac{\eta_{\text{SiO}^-} [\text{H}^+]_s}{\eta_{\text{SiOH}}}, \quad (15)$$

$$K_{a2} = \frac{\eta_{\text{SiOH}_2^+}}{\eta_{\text{SiOH}} [\text{H}^+]_s}, \quad (16)$$

$$K_m = \frac{\eta_{\text{SiOCa}^+} [\text{H}^+]_s}{\eta_{\text{SiOH}} [\text{Ca}^{2+}]_s}, \quad (17)$$

where η_i is the surface site density of the i^{th} functional group. $[\text{H}^+]_s$ and $[\text{Ca}^{2+}]_s$ are the surface molar concentrations of corresponding ions. To our knowledge, however, pH regulation and Ca^{2+} adsorption have not been used for modeling electrokinetic phenomena. Thus we combined models for protonation⁵⁴ and Ca^{2+} adsorption,⁵⁰ for which the total density of sites on the silica surface that can support chemical reactions is given by

$$\eta_{\text{Total}} = \eta_{\text{SiOH}} + \eta_{\text{SiO}^-} + \eta_{\text{SiOH}_2^+} + \eta_{\text{SiOCa}^+}, \quad (18)$$

From this equation, the effective surface charge density can be determined by

$$\sigma_s = -F\eta_{\text{Total}} \frac{K_{a1} - K_{a2}[\text{H}^+]^2 - K_m[\text{Ca}^{2+}]}{K_{a1} + [\text{H}^+] + K_{a2}[\text{H}^+]^2 + K_m[\text{Ca}^{2+}]}, \quad (19)$$

Eq. 19 serves is used in the Neumann condition defined in Eq. 11. Additional parameters for the model are provided in Table S1.

3.3.2 Finite element solution of PNP equations

The Poisson-Nernst-Planck (PNP) equations in the present study were numerically solved via the finite element method (FEM) using the commercial finite-element COMSOL (www.comsol.com) package and the free open-source FENICS⁵⁵ library. For all two dimensional (2D) geometries we considered (see Fig. S4), the PNP equations were solved by COMSOL with full pH-/adsorption regulated surface charge density to ensure consistency with prior studies of ion conductance in nanomaterials.^{6,56,57} For computational expenses reasons, we utilized the finite element method (FEM) package FENICS to solve the PNP equations, assuming first order Lagrange bases and default solver parameters. To simplify the boundary conditions, the Grahame equation was used to relate the surface charge density to the electric potential at the silica wall, which for a monovalent salt is given by

$$\sigma_s(\phi_0) = \sqrt{8c_0\epsilon_o\epsilon_r k_B T} \sinh\left(\frac{e\phi_0}{2k_B T}\right), \quad (20)$$

where ϕ_0 is the electric potential at the pore surface (for divalent salt, e.g., CaCl_2 , the corresponding Grahame equation is given as Eq. S1).⁵⁴

3.3.3 Conductivities and permeabilities of unit cells and bulk material

For numerical estimation of the KCl ionic conductance in nanoporous media, we evaluated the following conductance relationship proposed by Yeh et al:⁶

$$S = \frac{I}{\delta V} = \frac{F\langle J \rangle_{\Gamma}}{V_a - V_b}, \quad (21)$$

$$\langle J \rangle_{\Gamma} \equiv \sum_{i=1}^N \int_{\Gamma} J(\Gamma)_i d\Gamma, \quad (22)$$

where J_i , the flux density for species i , is computed from steady-state solutions to Eq. 8, V_a and V_b are the average electric potentials at the two ends of nanopore ($V_a - V_b$ value is close to applied potential bias $\delta\phi = 0.2V$, see Table S2), N is number of ion species, F is Faraday's constant, Γ is the cross-sectional surface within the nanopore center. The flux density was either provided directly from COMSOL or estimated from FENICS steady-state solutions using PARAVIEW.⁵⁸ For the CaCl_2 conductance in a nanochannel (length=5mm, width=30 μm and Height=18nm⁵²), we utilized a 2D model represented, given that width \gg height. We assumed $G_{final} = G_{slit}W10^{-4}$, where G_{slit} is the ionic conductance of the 2D nanoslit, W is the width of the 3D nanochannel. The division by 1.0000×10^4 reflects that our simulated domain was of length 5×10^{-7} m versus the 5×10^{-3} m channel used in Feust et al;⁵² despite this approximation, we found reasonable agreement between our predictions and experimental data.

Similarly, the membrane permeability, P_{eff} , and effective diffusion constant, D_{eff} , were evaluated as:^{59,60}

$$P_i = \frac{K_i D_{i,\text{eff}}}{L_m} \quad (23)$$

$$D_{i,\text{eff}} = \frac{\langle J_i \rangle L_x}{[i]_{\text{bulk}}} \quad (24)$$

where K_i and $D_{i,\text{eff}}$ are the partition coefficient and effective diffusion constant of each species in membrane, respectively. L_m is the thickness of membrane, $\langle J_i \rangle$ is the average flux density over the cross-section area at the middle of membrane (calculated in the same way as V_a and V_b evaluations mentioned above), L_x is the length along diffusion direction (defined as the distance between the external ends of two reservoirs) and $[i]_{\text{bulk}}$ is the bulk concentration. The value of K_{CF} in silica membrane is assumed to be 1×10^{-3} , which lies in the range of small organic molecules.⁵⁹

3.4 Extrapolation of effective conductivity estimates on EM-imaging data

In the final step, partial differential equation predictions of effective transport parameters are extrapolated onto the original EM-resolved structure. Given that each filter 'hit' represents a match for an entire unit cell, we the transport parameter estimated for the corresponding filter to a region commensurate in size to the unit cell. In regions that did not contain an obvious filter match, we assigned a permeation value that was intermediate to the fused and bulk pore

unit cells, as the unclassified regions still presented porous features that could permit substrate diffusion. In this case, the effective permeation, P_{eff} , for the entire material surface is determined by a surface area-weighted (Γ) average of the parameters determined for the different unit cell types, e.g.

$$P_{\text{eff}} = \frac{1}{\Gamma_{\text{tot}}} \sum_i \Gamma_i s_i \quad (25)$$

where i corresponds to the fused pore, bulk and unclassified regions.

4 Results and Discussion

4.1 Automated feature detection and mesh generation for oriented porous films

4.1.1 Application to EM-derived nanofilm data

A key contribution from our workflow presented in Fig. 1 is the automated detection of prominent structural features in imaged nanoporous films. In the Methods section, we outlined our procedure for generating matched filters representative of bulk (hexagonal closed packed) regions and fused pore defects. We note that the postulated fused pore is one of several types of defects evident in the data and that additional matched filters would be required to detect those features. However, given the lack of data for adequately training the matched filters for each defect type, we limit our approach to fused pores, which are somewhat prevalent in the EM image (Fig. 3B). Here we tested the performance of these data-derived filters on subsections of the raw EM data that were not used for filter training. Namely, in Fig. 3 we present a roughly 100nm by 100nm region that contains diagonal striations that we attribute to fused pore features. In the top two rows of Fig. 3, we show the rotated filters (left column) as well as the corresponding matched filter outputs (right column) for the fused pore filter. In the bottom row we denote the raw data used for the feature detection, as well as the above-threshold regions from all pore rotations indicated in red or green for the bulk and defect filters, respectively. Analogous results are presented for EM data that predominantly contain bulk (HCP) surface features in Fig. S3. The marked results in Fig. 3 and Fig. S3 suggest that the matched filtering protocol is able to detect and classify the bulk and fused pore features, though exact quantification of the accuracy is difficult given the resolution of the EM data. We note that there are several regions in the image that were not classified by either filter. By visual inspection, those regions present surface features that neither appear fused nor adhere to an HCP configuration. In principle, these unclassified regions could be used to train additional filters to facilitate complete characterization of the EM surface. We also found that tuning the threshold parameters was necessary to optimize the matched filtering results. Nevertheless, these data indicate 1) that filter rotation in ten degree increments is sufficient to reliably identify data features independent of their orientation and 2) that bulk and fused pore defect regions can be automatically detected in the raw test data.

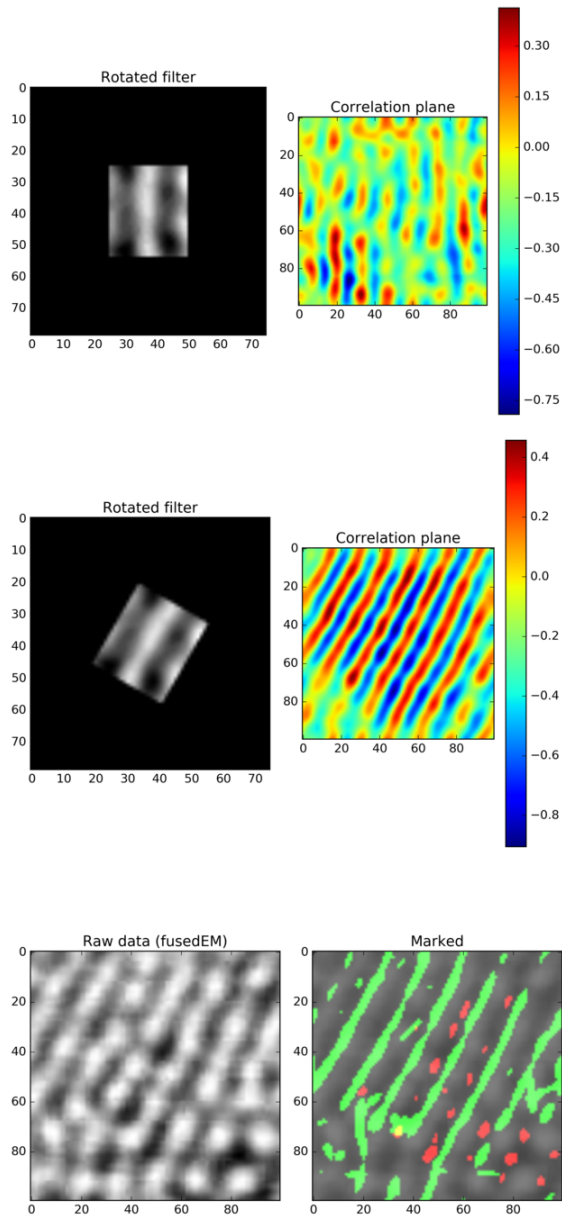


Figure 3: Matched filtering results for simulated transmission electron microscopy (TEM) images of a mesoporous silica film from Wooten et al.⁴² First and second rows correspond to the filters and corresponding matched filtering result at 0 and 30 degree rotations. Bottom row provides the raw data and an image denoting match filter detected fused pore (green) and bulk unit cell (red) features. Similar results are presented in Fig. S3, using raw data containing mostly bulk unit cell features .

4.2 Electrokinetic model of transport in oriented mesoporous films and other porous media

4.2.1 KCl conductance in mesoporous silica.

The intermediate stages of the Fig. 1 workflow entails estimation of effective transport parameters including conductivity (S_{eff}) and effective diffusivities (D_{eff}) or permeabilities (P_{eff}) for ionic species, given 3D representations of the porous features identified in the EM film data. These features include a perfectly cylindrical pore corresponding to the HCP bulk unit cell (Fig. 2A) and a 'slit-like' geometry representing fused pores that traverse the entire film depth (Fig. 2B). The dimensions of the two unit cells were determined by the segmentation procedure. The length and width of hexagonal unit cell were determined to be 31nm and 16nm and four one-half nanopores centered on each edge, for which each pore has a radius of 5nm. The length of fused pore unit cell was set to 30nm, while the width consisting of a 15nm slit formed by the fusion of two pores (represented by two red circles in Fig. 2B) centered between two 13.5nm wide impermeable regions. While the fused pore feature in principle could reflect a cylindrical pore oriented parallel to the film surface, it would not conduct ions traversing perpendicular to the film thus we do not explicitly consider this morphology.

A focal point of this section is the validation of our implemented model against several experimental assays of electrolyte conductance in nanochannels or nanoslits,^{7,52} in order to establish confidence in its application to a distinctly different morphology: mesoporous films. In this section, we describe the computational modeling of KCl and CaCl₂ diffusion in several nanoporous silica morphologies, as well as nanochannels and nanoslits previously characterized in the literature.^{7,52} We additionally consider mesoporous silica films synthesized and characterized by Wooten et al.⁴² All systems are modeled subject to voltage gradients or concentration gradients for measuring conductance or diffusion properties, respectively, under a broad range of ionic strengths. In concurrence with prior studies,^{6,8,56,57} we describe the electrokinetic mass transport using the PNP model under steady-state conditions, whereby the electrostatic field (ϕ) and electro-diffusion of electrolytes are coupled and solved simultaneously (Eq. 8). We further include reaction terms reflecting proton and metal equilibria with the silanol-terminated silica surface (Eq. 12 and Eq. 14), which together determine the surface charge density governing the PNP model (Eq. 19). While prior computational studies have characterized aspects of conductance in nanochannels and nanoslits,^{6,57} in this study we examine such transport phenomena in defect-containing mesoporous silica films.

The pH-dependence of surface charge has been well-described in prior works,⁶⁻⁸ and we include in Supplemental Section Sect. S.2.3 a validation of our model against an established theoretical model of pH-dependent surface charge density.⁵⁴ Namely, we verify that the negative surface charge of silica is reduced from $-115C/m^2$ expected at $[KCl] = 1M$ upon protonation with decreasing pH. Moreover, the extent of charge neutralization 1) decreases with increasing ionic strength of the background electrolyte KCl, and 2) these trends are comparable for film surfaces (planar) as well as film pores.

Using the validated pH-dependent PNP model, we predicted the conductance of a KCl solution (H^+ , OH^- , K^+ and Cl^-) through a single 34nm nanopore of radius 5.1nm at pH=7.5 and pH=5, assuming a 2D axially-symmetric domain. These conditions mirror those considered by Yeh et al.,⁶ although their model additionally included a modified Stokes component to capture electroosmotic

flow. Consistent with experimental measurements from Smeet et al⁷ and Yeh et al,⁶ the model predicts that conductance scales with concentration at higher ionic strengths, as the electric potential of the channel walls are largely shielded by short Debye lengths. We note that while the Smeets et al⁷ study reports findings based on a roughly neutral pH, we found that pH=5 was necessary to recapitulate those findings, and further, the conductance data resemble those from a related experiment conducted at pH=5.⁸ In Fig. S10, we additionally demonstrate that the addition of electroosmotic effects by way of Stokes as done by Yeh et al⁶ has a negligible impact on the conductance results, which supports our omission of osmotic flow from our simulations. Regardless of pH, the predicted conductance data show similar declines in conductance from 1×10^{-3} to 1M, which suggests that the contribution of surface charge is negligible at higher ionic strengths. In other words, the channel flux is largely dependent on the applied field parallel to the channel and that electrostatic interactions within the channel are of little consequence under these conditions. At lower ionic strengths, conductance is dictated by surface charge owing to the overlapping of electric double layers, however the pH mitigates this effect by attenuating the net negative charge of the boundary. We found analogous trends for a 3D nanopore domain the HCP unit cell assuming a fixed (pH independent) surface charge.

The change in conductance can be rationalized based on the fluxes of each ionic species, which arise due to concentration gradients (first term in the right hand side of Eq. 8) and electro-diffusion (second term of Eq. 8). For the latter of which, the amplitude decreases as a function of concentration (see Fig. S5), which ultimately determines the overall conductance. It is worth noting that the effect of the potential gradient along the pore wall on ion diffusion is akin to widening or constricting the pore radius for counter- or co-ions, respectively. This is apparent from the data in Table S3, for which we provide species-dependent flux densities and ionic conductances for different surface charge potentials at $\kappa D = 1.06$ and 3.35 , assuming $[KCl] = 1\text{mM}$ or 10mM for the 10.2nm diameter (D) nanopore. These data reflect that increasing the magnitude of the negative wall potential increases K^+ flux by about 60% while decreasing Cl^- by 50%, leading to an overall increase in conductance of 50%. Further, increasing ionic strength supports ten-fold increases in K^+ and Cl^- fluxes, giving a five fold increase in conductance overall.

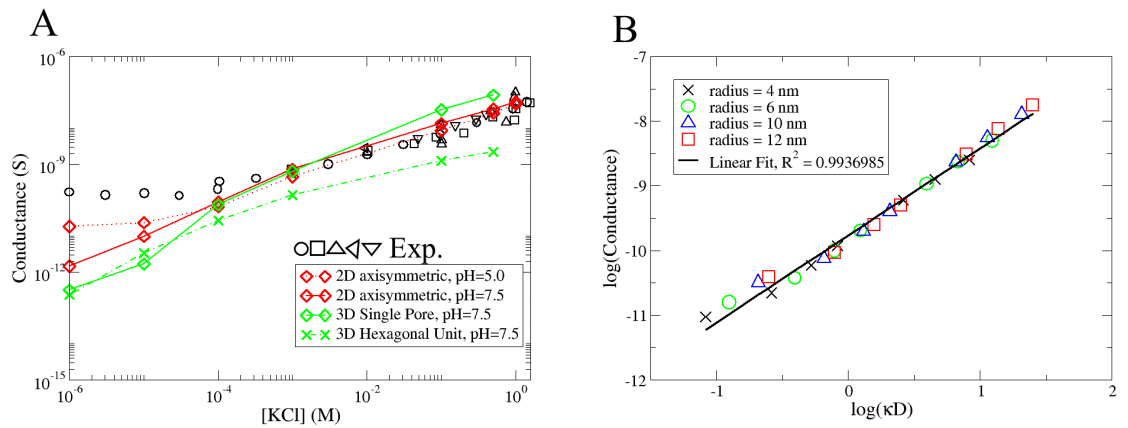


Figure 4: KCl ionic conductance in a nanopore. A) Comparison between experimental data and numerical results. For the 2D axisymmetric pore, the full PNP pH/adsorption model was used while for the 3D nanopore, the PNP was solved with fixed electric potential (values are from 2D results) applied at nanopore wall. Black symbols designate experimental KCl conductance data for a 34 nm silica nanopore of radius 5.1 nm (pH=7.5) from.⁷ B) Ionic conductance of nanopore (2D axisymmetric, pH=7.5) at varying radii and bulk [KCl] (expressed as κD , $D=10.2\text{nm}$ is the diameter of nanopore).

Interestingly, when these conductance data are represented as a function of the dimensionless parameter κD , the trends scales as $\log(S)$ versus $\log(\kappa D)$, as shown in Fig. 4B. This trend is observed both when ionic strength is varied from 1×10^{-2} to 80mM for fixed pore radii (4-12 nm), as well as when radii are varied for a fixed ionic strength. The latter variation supports the notion that the presence of surface charge on the pore boundary essentially modulates the effective pore diameter. Note that this κD dependence breaks down for variable (e.g. pH-dependent) surface charges at low ionic strength ($\kappa \rightarrow 0$). We anticipate that this behavior depend on the assumed surface potential, based on analyses in Sect. S.4 that demonstrate predicted conductances smoothly decrease as the negative wall potential was varied toward positive potentials.

4.2.2 CaCl_2 transport and adsorption

In the preceding section, we demonstrated agreement between numerical predictions of KCl conductance in several nanoporous geometries, for which the surface charge is dependent on pH but independent of K^+ . We now consider the extent to which an adsorbable ion can compete with protonation and thereby influence ion conduction. Specifically, we consider Ca^{2+} adsorption to the surface, which has been shown to be significant^{8,52} and a necessary factor in conductance models to recapitulate experimental data^{7,61}. Accordingly, we include in Eq. 19 Ca^{2+} surface adsorption, assuming equilibrium constants in the micromolar range. For validating the CaCl_2 model, we refer to CaCl_2 ionic conductance data collected from a 'nanoslit' with a length of 5mm, width of $30\mu\text{m}$ and height of 18nm, respectively (Fuest et al⁵²). Here we assume a 2D domain in Cartesian space (length versus height), given that the width is much greater than the height. Further, since at steady state the ionic conductance of a nanochannel is inversely proportional to the length of the nanochannel,⁶² we assumed a slit length of 500 nm instead of 5 mm for reasons of computational expense(Fig. S4). The simulation domain in this example contains four ion species: H^+ , OH^- , Ca^{2+} and Cl^- .

Simulated and experimentally-measured conductances are reported in Fig. 5 for PNP models with and without Ca^{2+} adsorption. Analogous to our simulations for KCl, at low pH (pH = 5), we note that conductance (in log units) decreases linearly with $\log[\text{CaCl}_2]$ for calcium chloride concentrations of 1 mM and higher, in agreement with experiment. Since the conductivities predicted among the surface charge models were comparable, it is expected that the pH and Ca^{2+} do not significantly modulate the surface charge density for CaCl_2 above 1 mM. As the concentration is decreased below 1 mM, however, the rate of decrease in conductance slows and approaches a minimum at approximately 100 μM , below which conductance accelerates with decreasing ionic strength. This is attributed to the fact that at low ionic strength, protons are more effective in neutralizing wall charge. Both the pH and pH+Ca-dependent surface charge models capture this behavior to an appreciable degree, although they do not capture the magnitude of the conductance increases exhibited in the experimental data. We attribute this discrepancy in part to the uncertainty in the parameters η_{total} , pK_a , pK_b and pK_m . We attribute the experimentally-observed trends at low ionic strength to the increased involvement of pH in regulating the surface potential, as discussed in.^{53,63} Namely, as the ionic strength of the solution is decreased, protons have a higher tendency to be attracted to the negatively charged slit walls, upon which they neutralize the negative wall charge.

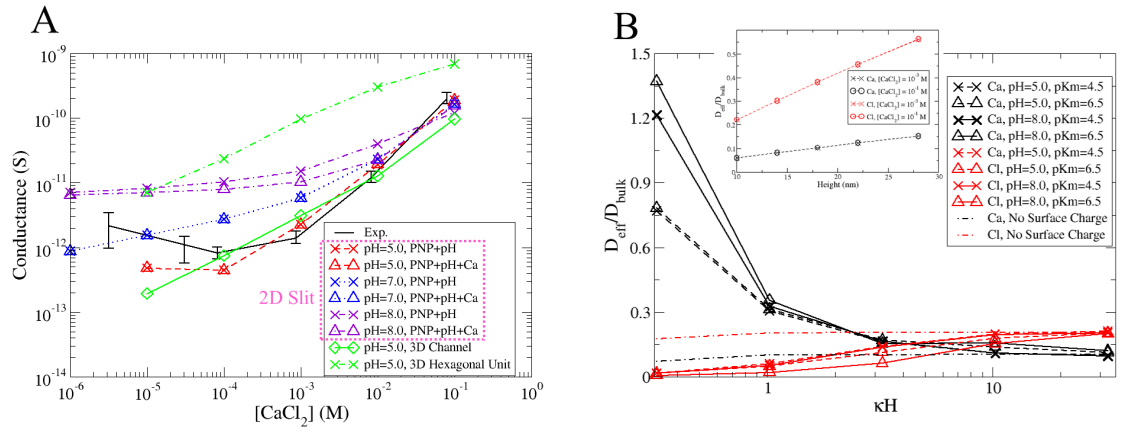


Figure 5: Comparison of $CaCl_2$ ionic conductance between numerical and experimental data. The length(L), width(W) and height(H) of the nanochannel are $L=5mm$, $W=30\mu m$ and $H=18nm$, respectively.⁵²(A) Experimental and numerical conductance as a function of $[CaCl_2]$. PNP+pH: pH regulated surface charge density. PNP+pH+Ca: pH regulated surface charge density plus Ca^{2+} adsorption. (B) Effective diffusion constant of Ca^{2+} and Cl^- versus $[CaCl_2]$ (expressed as κH , $H=18nm$ is the height of nanochannel/nanoslit) under different Ca^{2+} adsorption constants and pHs. The inset denotes the effective diffusion constant at varying nanoslit heights when no surface charge density is present.

Apparent from these data is that Ca^{2+} adsorption has an insignificant contribution to the conductance, except at basic pHs. Accounting for Ca^{2+} adsorption decreases the conductance modestly relative to the basic PNP+pH model. To rationalize this behavior, in Fig. 5B we present effective diffusion constants for Ca^{2+} and Cl^- as functions of ionic strength, pH and adsorption equilibrium constants. At high ionic strength, D_{eff} s for both ions approach limits predicted for neutral pores, with Cl^- presenting 20% of its bulk diffusion rate compared to about 10% for Ca^{2+} . As the ionic strength is reduced, the Cl^- D_{eff} declines to nearly negligible values at $[\text{CaCl}_2]=1 \times 10^{-6}$ M, while that of Ca^{2+} increases by nearly eight-fold, hence in this regime the current predominantly arises due to cation flux. Further, these trends are modestly attenuated as pK_m is reduced at basic pH to reflect increased Ca^{2+} adsorption, as the adsorbed Ca^{2+} ions partially neutralize the attractive, negative silica wall surface charge that would otherwise facilitate Ca^{2+} diffusion. Under acidic conditions, this distinction is lost as there are fewer sites available to accommodate Ca^{2+} relative to protons. Hence, the drop in conductance shown in Fig. 5 could be attributed to a reduction in the Ca^{2+} D_{eff} as Ca^{2+} surface binding increases. We emphasize here that our model of Ca^{2+} adsorption only modulates surface charge and therefore neglects changes to the free Ca^{2+} in the channel interior. We justify this assumption by noting that adsorbed Ca^{2+} comprises a small percentage of the total Ca^{2+} in the nanopore, given the large nanopore radius relative to the adsorption layer (see Sect. S.4.1).

4.3 Small charged molecule permeation properties of a mesoporous silica film

4.3.1 Validation of PNP model for CF permeation in silica film

In the previous sections, implementations of the PNP equations were validated against experiment and simulation studies for several nanoporous silicate geometries. Here we utilize PNP simulations to explore permeation properties of small ligands in a oriented mesoporous film,⁴² for which TEM provides a distribution of bulk and defect features (Fig. 3b) A key difference between these geometries and those considered in the prior sections is that the porous silica membranes here present a multitude of densely packed pores. We first validate our model by simulating permeation properties of 5(6)-Carboxyfluorescein (CF) in the Wooten et al⁴² membranes. Based on their experimental setup, the length (thickness of membrane) and radius of the nanopore is set as 90nm and 5nm, respectively. The pH is set as 7.4 (all CF numerical simulations were conducted at pH=7.4 unless otherwise stated) and background [KCl] is set as 0.9M to mimic the ionic strength (0.9M, $\kappa D=31.8$) in experimental setup. At this basic pH, CF is expected to form the anion CF^- ($pK_a=6.5$) and thus we do not anticipate adsorption of the small molecule. Our model consists of five ionic species H^+ , OH^- , Cl^- , K^+ and CF^- , for which we assume an absorbing boundary condition for CF on one reservoir edge (e.g. $[\text{CF}]=0$).

As shown in Fig. 3B, although the nanopores are mainly in hexagonal packing arrangement, structural defects such as fused nanopores are evident. To resemble the real membrane composition, we thus consider two unit cell structures appeared in the TEM image: a hexagonal unit cell and a fused pore unit cell (dimensions are shown as in Fig. 2). The permeabilities of CF for these two unit structures were predicted to be 1.12×10^{-6} m/s and 1.185×10^{-6} m/s, re-

spectively (see Fig. S13) and modestly less than the experimentally-determined value of approximately 1.4×10^{-6} m/s.⁴² Not unexpectedly, the difference in the unit cell permeabilities can be explained by the relative porosities (see Fig. S14), with the fused pore have a greater cross-sectional area than the HCP cell (0.357 and 0.317, respectively). Unlike in Fig. S13, for which we used a background ionic strength as 0.9M to mimic the experimental setup in Wooten et al,⁴² here we used a range of dilute ionic strengths. The motivation for dilute conditions is two-fold: 1) high ionic strength has a strong electrostatic screening effect which undermines the influence of wall electric potential on CF permeation and 2) it has been shown surface charge density/electric potential begins to dominate ionic transport when bulk concentration is smaller than 1mM.⁵² As shown in Fig. 6, for a fixed surface potential, both hexagonal and fused pore unit cells present larger CF permeabilities as ionic strength is increased. The increase with $\log(\kappa D)$ plateaus when the Debye length is much smaller than D , under which case the permeability is nearly completely determined by the pore diameter. These permeabilities indicate that the higher background ionic strength attenuates the repulsive interaction between anionic CF and the negatively-charged nanopore wall, thus leading a larger CF permeation. Analogously, for a given ionic strength, decreasing the magnitude of the electric potential permits greater CF permeability. These effects become more apparent as ionic strength is reduced, and moreover, the differences in permeabilities for the respective unit cells magnify.

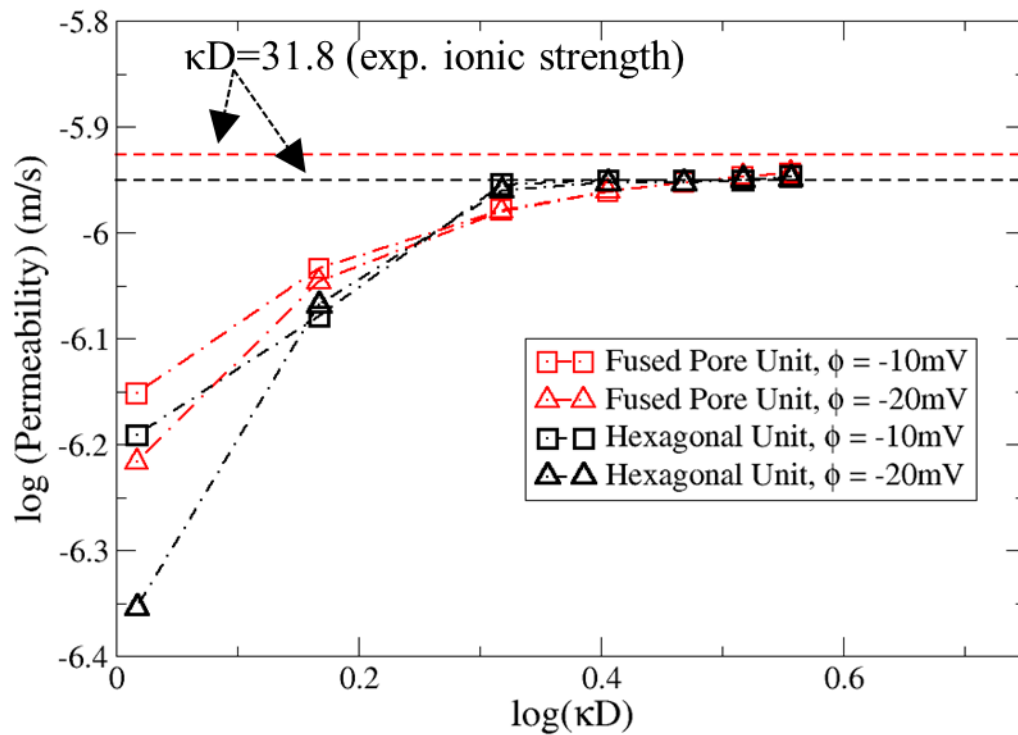


Figure 6: Permeability of CF in hexagonal and fused pore unit cells vs. κD ($D=10\text{nm}$ is the diameter of pore) under different wall electric potentials when $\text{pH}=7.4$ and $[\text{CF}]=1\text{mM}$. The two straight dashed lines denote predicted CF permeabilities under 900mM background ionic strength ($\kappa D = 31.18$, see Fig. S13 for details) .

Case	S.A. (%)			P_{eff}
	Bulk	Fused	Uncharacterized	
Fused pore-rich	0.05	88.9	0.06	$6.0 \times 10^{-1} \mu\text{m s}^{-1}$
Bulk-like	0.28	0.44	0.28	$5.5 \times 10^{-1} \mu\text{m s}^{-1}$
Exp				$1.4 \mu\text{m s}^{-1}$

Table 1: Effective permeabilities, P_{eff} , for the fused pore-rich and bulk-like regions of Fig. S2, as computed by Eq. 25. Predicted conductivities for bulk and fused unit cells are from Fig. 6 and their surface area weights are estimated from matched filter detections in Fig. 3 and Fig. S3.

In support of the final step of the work flow in Fig. 1, we interpolate these permeability predictions for the fused pore ($6.2 \times 10^{-1} \mu\text{m s}^{-1}$) and the bulk HCP pore ($4.5 \times 10^{-1} \mu\text{m s}^{-1}$) unit cells onto the matched filtered data from Fig. 3. Since the matched filtering provides a quantitative means of estimating the propensity of detected defects relative to bulk, the effective permeability of the entire EM film can be approximated by surface area-weighted conductivities of the corresponding unit cells. While in principle the conductivities between adjacent unit cells could be coupled and thus disfavor this simple extrapolation approach, given the modest surface potentials we assumed that the conductivity of a given unit cell was independent of its neighbors. In Table 4.3.1 we summarize these data for the fused pore-rich and bulk-like regions. The fused pore-rich region presents roughly 90% fractional surface area attributed to fused pore unit cells, thus the P_{eff} of $6 \times 10^{-1} \mu\text{m s}^{-1}$ approaches P_{eff} predicted for a single fused pore. For the bulk-like region, the surface area was split between bulk-like, fused pore, and uncharacterized unit cells, and thus yielded an intermediate P_{eff} of $5.5 \mu\text{m s}^{-1}$. Surprisingly, the bulk-like unit cells did not contribute the majority of the surface, but instead, a significant percentage was unclassified despite resembling the bulk HCP form by visual inspection. Upon investigating the correlation outputs corresponding to the unclassified cells, we found that relative spacing between pores were dilated, which arguably led to a reduced overlap of the HCP pore filter. We anticipate that augmenting the rotated filter bank with dilations and contractions of the 'typical' unit cell could potentially improve detection for such cases.

4.3.2 Exploiting surface interactions to tune permeation rates

Factors controlling CF permeation In this section, we examine how CF permeation can be controlled by ionic strength, nanopore wall surface charge density, electric potential and selective CF binding. In Fig. 7 we demonstrate ion permeabilities as a function of ion size and ion/wall electrostatic interaction energy. Not surprisingly, the permeability decreases with effective pore radius, which represents the difference between the actual pore radius and that radius of a permeant ion (e.g. $r_{\text{eff}} = r_{\text{pore}} - r_{\text{ion}}$). In other words, as the ion size is increased, the effective pore radius decreases and smaller permeabilities result. We note that as the ion size approaches that of the pore, additional factors would likely have to be added to the model to accurately model the ion/wall interactions, including hydrodynamic interactions and potential changes in local diffusivity.⁶⁴ Similarly, increasing the repulsive interaction energy decreases permeability, while attractive energies increase permeation. The effects of electro-

static interactions attenuate with increasing ionic strength, as shown for CaCl_2 effective diffusion rates in Fig. 5b.

As shown in Fig. 7B, at modest ionic strengths (100 mM), the capacity to modulate ion transport by charge is diminished, as the predicted permeabilities at 100 mM are constant across the range of electrostatic interaction energies considered, compared to the 1 mM data. If instead one modified the surface chemistry to selectively bind a substrate, the loss in electrostatically-driven selectivity commonly observed at higher loadings (ionic strength)⁶⁵ could be circumvented. We illustrate this by assuming there exists a buffer that selectively binds CF, which in principle could arise through adding appropriate functional groups to the silica surface or tethering a binding agent to the pore wall.^{66,67} For simplicity, we assume rapid equilibrium for this potential reaction, that is, the binding/dissociation between CF and buffer occur more rapidly than the timescale of diffusion. Under this limit, the local diffusivity of CF in the buffer region (D_{buffer}) can be described by:⁶⁸

$$D_{buffer} = D_{free} \left(1 + \frac{K_s[B]}{(K_s + [CF])^2} \right)^{-1} \quad (26)$$

where K_s is the dissociation constant, $[B]$ is concentration of buffer and D_{free} is the diffusion constant without any buffer. We model the effects of this rapid equilibrium by altering the local diffusion constant used in the PNP equation (Eq. 8), which effectively reduces the net flux with increasing buffer concentration and CF binding affinity. As shown in Fig. 7B, a buffer concentration $[B]=1\text{mM}$ (comparable to $[CF]$), the permeability is reduced by 6.27% compared to the absence of buffer. As $[B]$ is increased to 10mM and 100mM, the permeability is further reduced to 27.6% and 39.0%, respectively. Overall, these data suggest that considerable flexibility in tuning permeation properties in these mesoporous films may be realized, though exploiting combinations of altered pore sizes,^{69,70} tuning ionic strength/loading rates,⁶⁹ or introducing ion-specific surface chemistry.^{67,71}

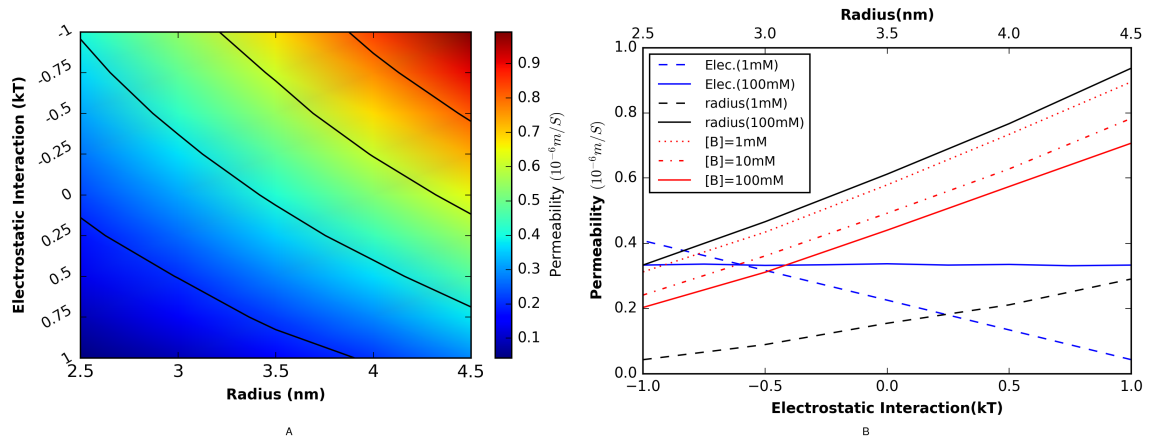


Figure 7: A) Numerically simulated CF permeability in hexagonal unit cell as a function of electrostatic interaction energies and pore radii. Background ionic strength and bulk [CF] are both set as 1mM. B) CF permeability at fixed pore radii (2.5nm) and fixed electrostatic interaction energy (1kT) under different background ionic strength. Red lines denote CF permeability when a 1nm thick buffer layer present along the inner wall of pore, the local diffusion constant of CF is given as Eq. 26 where K_s is assumed to be 1. The dots, dashed and solid red lines depict buffer concentration [B]=1mM, 10mM and 100mM, respectively.

5 Conclusions

In this study, we have developed and explored the utility of a workflow for automatically characterizing EM microscopy data of mesoporous silica films and performing detailed ion transport simulations of both bulk and defect mesocrystalline features. A primary innovation in this method is the use of a matched filter approach to robustly detect known features in electron microscopy data. The procedure relies on a bank of filters for which the EM signature of a given defect is known, as well as rotated versions of those filters. Our results demonstrate that both bulk and fused features could be determined with high selectivity. We emphasize that our matched filtering approach is rather simple, but can be easily extended to incorporate sundry developments in matched filter theory to improve the accuracy and reliability of detecting diverse signals in EM data.

To simulate ion transport in these silica-based materials, we implemented a PNP model that includes pH and Ca^{2+} adsorption regulation of pore charge density. Our models confirm that electrolyte conductance in mesoporous silica films is dependent on ionic strength, surface charge, pH, and adsorption kinetics, as has been already demonstrated for single nanoporous channels and slits. Under some conditions, the effects of ionic strength on transport can be described as an effective pore radius that reflects the solution Debye length. We extended these simulations to include a small molecule, CF, and identified parameters under which CF transport could be optimized through variation of porosity, surface charge and selective CF binding. In our approach, we assumed a rapidly-equilibrating buffering zone, that notably reduced the apparent diffusion coefficient of the selected-for ion, thus leading to smaller transport properties. Lastly, we leveraged simulation results of representative unit cells derived from the EM microscopy data to estimate effective CF permeation rate for the mesoporous silica membrane surface. Overall, the workflow in Fig. 1 that we establish in this study and validate, where possible, has strong potential to benefit the characterization of effective transport properties in increasingly complex composite materials, including those with hierarchical degrees of structures, and especially materials significant incidents of defects that perturb substrate diffusion.

6 Acknowledgments

This article is dedicated to William A. Goddard, III, for his continual scientific inspiration and guidance throughout PKH's career. Research reported in this publication was supported by the Maximizing Investigators' Research Award (MIRA) (R35) from the National Institute of General Medical Sciences (NIGMS) of the National Institutes of Health (NIH) under grant number R35GM124977. PKH also thanks Dr. Beth Gupton for helpful discussions regarding the electron microscopy data.

References

- [1] P. Innocenzi and L. Malfatti. “Mesoporous thin films: properties and applications”. In: *Chem. Soc. Rev.* 42 (9 2013), pp. 4198–4216.
- [2] M. Hartmann. “Ordered Mesoporous Materials for Bioadsorption and Biocatalysis”. In: *Chemistry of Materials* 17.18 (2005), pp. 4577–4593.
- [3] J.-F. Chen et al. “Preparation and characterization of porous hollow silica nanoparticles for drug delivery application”. In: *Biomaterials* 25.4 (2004), pp. 723–727. ISSN: 0142-9612.
- [4] T.-L. Chew, A. L. Ahmad, and S. Bhatia. “Ordered mesoporous silica (OMS) as an adsorbent and membrane for separation of carbon dioxide (CO₂)”. In: *Advances in Colloid and Interface Science* 153.1 (2010), pp. 43–57. ISSN: 0001-8686.
- [5] J. Persello and E. Papirer. “Surface and Interface Structure of Silicas”. In: *Adsorption on Silica Surfaces* 10 (2000), pp. 298–339.
- [6] L. H. Yeh, M. Zhang, and S. Qian. “Ion transport in a pH-regulated nanopore”. In: *Analytical Chemistry* 85.15 (2013), pp. 7527–7534. ISSN: 00032700.
- [7] R. M. M. Smeets et al. “Salt dependence of ion transport and DMA translocation through solid-state nanopores”. In: *Nano Letters* 6.1 (2006), pp. 89–95. ISSN: 15306984.
- [8] C. Duan and A. Majumdar. “Anomalous ion transport in 2-nm hydrophilic nanochannels”. In: *Nature Nanotechnology* 5.12 (2010), pp. 848–852. ISSN: 1748-3387.
- [9] K. P. Singh and M. Kumar. “Effect of Nanochannel Diameter and Debye Length on Ion Current Rectification in a Fluidic Bipolar Diode”. In: *The Journal of Physical Chemistry C* 115.46 (2011), pp. 22917–22924.
- [10] H. Daiguji, P. Yang, and A. Majumdar. “Ion Transport in Nanofluidic Channels”. In: *Nano Letters* 4.1 (2004), pp. 137–142. ISSN: 15306984.
- [11] R. B. Schoch, J. Han, and P. Renaud. “Transport phenomena in nanofluidics”. In: *Rev. Mod. Phys.* 80 (3 July 2008), pp. 839–883.
- [12] C. C. Chang et al. “Numerical simulation of proton distribution with electric double layer in extended nanospaces”. In: *Analytical Chemistry* 85.9 (2013), pp. 4468–4474. ISSN: 00032700.
- [13] S. Atalay, L. H. Yeh, and S. Qian. “Proton enhancement in an extended nanochannel”. In: *Langmuir* 30.43 (2014), pp. 13116–13120. ISSN: 15205827.
- [14] L.-J. Cheng and L. J. Guo. “Rectified Ion Transport through Concentration Gradient in Homogeneous Silica Nanochannels”. In: *Nano Letters* 7.10 (2007). PMID: 17894519, pp. 3165–3171.
- [15] M. M. Yu, R. D. R. D. Noble, and J. L. J. L. Falconer. “Zeolite membranes: microstructure characterization and permeation mechanisms.” In: *Accounts of Chemical Research* 44.11 (2011), pp. 1196–1206.
- [16] Y. Yan, M. E. Davis, and G. R. Gavalas. “Preparation of highly selective zeolite ZSM-5 membranes by a post-synthetic coking treatment”. In: *Journal of Membrane Science* 123.1 (1997), pp. 95–103.

- [17] G. Bonilla et al. “Fluorescence confocal optical microscopy imaging of the grain boundary structure of zeolite MFI membranes made by secondary (seeded) growth”. In: *Journal of Membrane Science* 182.1-2 (2001), pp. 103–109. ISSN: 03767388.
- [18] N. John et al. “Evolution of Surface Morphology with Introduction of Stacking Faults in Zeolites”. In: *Chemistry - A European Journal* 16.7 (Feb. 2010), pp. 2220–2230. ISSN: 09476539.
- [19] H.-X. Zhou, G. Rivas, and A. P. Minton. “Macromolecular Crowding and Confinement: Biochemical, Biophysical, and Potential Physiological Consequences *”. In: *Annual Review of Biophysics* 37.1 (2008), pp. 375–397.
- [20] M. B. J. Roeffaers et al. “Morphology of Large ZSM-5 Crystals Unraveled by Fluorescence Microscopy”. In: *Journal of the American Chemical Society* 130.17 (2008), pp. 5763–5772.
- [21] J. M. Thomas and P. L. Gai. “Electron Microscopy and the Materials Chemistry of Solid Catalysts BT - (null)”. In: *Advances in Catalysis*. Vol. 48. Elsevier, 2004, pp. 171–227. ISBN: 9780120078486.
- [22] M. HUNGER et al. “Investigation of Internal Silanol Groups as Structural Defects in Zsm-5-Type Zeolites”. In: *Journal of the Chemical Society-Faraday Transactions I* 83 (1987), pp. 3459–&.
- [23] R. Valiullin et al. “Concentration-dependent self-diffusion of liquids in nanopores: A nuclear magnetic resonance study”. In: *Journal of Chemical Physics* 120.24 (2004), pp. 11804–11814. ISSN: 00219606.
- [24] S. Auerbach, J. Kärger, and S. Vasenkov. “Diffusion in zeolites”. In: (2003), p. 97.
- [25] W. Zhou and Z. Wang. “Scanning Microscopy for Nanotechnology: Techniques and Applications”. In: *Springer* (2006).
- [26] D. Z. Zhao et al. “Continuous Mesoporous Silica Films with Highly Ordered Large Pore Structures”. In: *Advanced Materials* 10.16 (1998), pp. 1380–1385.
- [27] B. Coasne et al. “Effect of Morphological Defects on Gas Adsorption in Nanoporous Silicas”. In: *The Journal of Physical Chemistry C* 111.43 (2007), pp. 15759–15770.
- [28] B. Coasne and R. J.-M. Pellenq. “A grand canonical Monte Carlo study of capillary condensation in mesoporous media: Effect of the pore morphology and topology”. In: *The Journal of Chemical Physics* 121.8 (2004), pp. 3767–3774.
- [29] S. K. Alexander et al. “SEM Image Analysis for Quality Control of Nanoparticles”. In: Springer, Berlin, Heidelberg, 2009, pp. 590–597.
- [30] C. Zhao and Y. Qiao. “Characterization of nanoporous structures: from three dimensions to two dimensions”. In: *Nanoscale* 8 (40 2016), pp. 17658–17664.
- [31] C. Hamngren Blomqvist et al. “Pore size effects on convective flow and diffusion through nanoporous silica gels”. In: *Colloids and Surfaces A: Physicochemical and Engineering Aspects* 484 (Nov. 2015), pp. 288–296. ISSN: 09277757.
- [32] T. R. Wojcik and D. Krapf. “Solid-state nanopore recognition and measurement using Shannon entropy”. In: *IEEE Photonics Journal* 3.3 (June 2011), pp. 337–343. ISSN: 19430655.

- [33] M. Okuda et al. “Structural analysis of rattle-type hollow mesoporous silica spheres using electron tomography and energy filtered imaging”. In: *Surface and Interface Analysis* 42.10-11 (2010), pp. 1548–1551. ISSN: 1096-9918.
- [34] J. Zečević, K. P. de Jong, and P. E. de Jongh. “Progress in electron tomography to assess the 3D nanostructure of catalysts”. In: *Current Opinion in Solid State and Materials Science* 17.3 (2013). Electron Tomography, pp. 115–125. ISSN: 1359-0286.
- [35] H. Daiguji. “Ion transport in nanofluidic channels”. In: *Chem. Soc. Rev.* 39.3 (Feb. 2010), pp. 901–911. ISSN: 0306-0012.
- [36] K. Shirono, N. Tatsumi, and H. Daiguji. “Molecular Simulation of Ion Transport in Silica Nanopores”. In: *The Journal of Physical Chemistry B* 113.4 (Jan. 2009), pp. 1041–1047. ISSN: 1520-6106.
- [37] S. Joseph and N. R. Aluru. “Hierarchical Multiscale Simulation of Electrokinetic Transport in Silica Nanochannels at the Point of Zero Charge”. In: *Langmuir* 22.21 (Oct. 2006), pp. 9041–9051. ISSN: 0743-7463.
- [38] P. E. M. Lopes et al. “Development of an Empirical Force Field for Silica. Application to the Quartz/Water Interface”. In: *The Journal of Physical Chemistry B* 110.6 (2006), pp. 2782–2792.
- [39] L.-H. Yeh et al. “Field Effect Control of Surface Charge Property and Electroosmotic Flow in Nanofluidics”. In: *The Journal of Physical Chemistry C* 116.6 (2012), pp. 4209–4216. ISSN: 1932-7447.
- [40] M. Barisik et al. “Size Dependent Surface Charge Properties of Silica Nanoparticles”. In: *The Journal of Physical Chemistry C* 118.4 (2014), pp. 1836–1842.
- [41] S. Atalay, L.-H. Yeh, and S. Qian. “Proton Enhancement in an Extended Nanochannel”. In: *Langmuir* 30.43 (2014), pp. 13116–13120.
- [42] M. K. Clark Wooten et al. “Synthesis and Nanofiltration Membrane Performance of Oriented Mesoporous Silica Thin Films on Macroporous Supports”. In: *ACS Applied Materials and Interfaces* 8.33 (2016), pp. 21806–21815. ISSN: 19448252.
- [43] H. L. Van Trees. *Detection, Estimation, and Modulation Theory, Part I*. New York, USA: John Wiley & Sons, Inc., Sept. 2001, p. 716. ISBN: 0471095176.
- [44] C. Geuzaine and J.-F. Remacle. “Gmsh: A 3-D finite element mesh generator with built-in pre- and post-processing facilities”. In: *International Journal for Numerical Methods in Engineering* 79.11 (2009), pp. 1309–1331. ISSN: 1097-0207.
- [45] T. Liao et al. “Multi-core CPU or GPU-accelerated Multiscale Modeling for Biomolecular Complexes.” In: *Molecular Based Mathematical Biology (Online)* 1 (July 2013), pp. 164–179.
- [46] H. Daiguji, P. Yang, and A. Majumdar. “Ion Transport in Nanofluidic Channels”. In: *Nano Letters* 4.1 (2004), pp. 137–142.
- [47] C.-Y. Lin et al. “Salt gradient driven ion transport in solid-state nanopores: the crucial role of reservoir geometry and size”. In: *Phys. Chem. Chem. Phys.* 18 (43 2016), pp. 30160–30165.

- [48] G. Mitscha-Baude et al. “Adaptive and iterative methods for simulations of nanopores with the PNP–Stokes equations”. In: *Journal of Computational Physics* 338.Supplement C (2017), pp. 452–476. ISSN: 0021-9991.
- [49] L.-H. Yeh et al. “Gate manipulation of ionic conductance in a nanochannel with overlapped electric double layers”. In: *Sensors & Actuators: B. Chemical* 215 (2015), pp. 266–271.
- [50] S. Datta et al. “Effect of divalent ions on electroosmotic flow in microchannels”. In: *Mechanics Research Communications* 36.1 (2009), pp. 65–74. ISSN: 00936413.
- [51] B. J. Kirby and E. F. Hasselbrink. “Zeta potential of microfluidic substrates: 1. Theory, experimental techniques, and effects on separations”. In: *ELECTROPHORESIS* 25.2 (Jan. 2004), pp. 187–202. ISSN: 0173-0835.
- [52] M. Fuest et al. “Cation dependent transport in a field effect nanofluidic device”. In: *2015 Transducers - 2015 18th International Conference on Solid-State Sensors, Actuators and Microsystems (TRANSDUCERS)*. IEEE, June 2015, pp. 247–250. ISBN: 978-1-4799-8955-3.
- [53] F. H. J. Van Der Heyden et al. “Charge inversion at high ionic strength studied by streaming currents”. In: *Physical Review Letters* 96.22 (2006). ISSN: 00319007.
- [54] J. N. Israelachvili. *No Title*. Academic Press, 2011, p. 704. ISBN: 9780123919274.
- [55] M. Alnæs et al. “The FEniCS Project Version 1.5”. In: *Archive of Numerical Software* 3.100 (2015). ISSN: 2197-8263.
- [56] Y. Ma et al. “pH-regulated ionic conductance in a nanochannel with overlapped electric double layers”. In: *Analytical Chemistry* 87.8 (2015), pp. 4508–4514. ISSN: 15206882.
- [57] Y. Ma et al. “Programmable ionic conductance in a pH-regulated gated nanochannel”. In: *Physical Chemistry Chemical Physics* 16.37 (2014), p. 20138. ISSN: 1463-9076.
- [58] J. Ahrens, B. Geveci, and C. Law. “ParaView: An End-User Tool for Large Data Visualization, Visualization Handbook”. In: *Elsevier* (2005).
- [59] W. Stein. “Transport and Diffusion across Cell Membranes”. In: *Academic Press* (1986).
- [60] P. M. Kekenus-Huskey, C. E. Scott, and S. Atalay. “Quantifying the Influence of the Crowded Cytoplasm on Small Molecule Diffusion”. In: *The Journal of Physical Chemistry B* 120.33 (2016). PMID: 27327486, pp. 8696–8706.
- [61] L.-H. Yeh et al. “Field Effect Control of Surface Charge Property and Electroosmotic Flow in Nanofluidics”. In: *The Journal of Physical Chemistry C* 116.6 (2012), pp. 4209–4216.
- [62] R. Karnik et al. “Effects of Biological Reactions and Modifications on Conductance of Nanofluidic Channels”. In: *Nano Letters* 5.9 (2005). PMID: 16159198, pp. 1638–1642.
- [63] R. Karnik et al. “Effects of biological reactions and modifications on conductance of nanofluidic channels”. In: *Nano Letters* 5.9 (2005), pp. 1638–1642. ISSN: 15306984.

- [64] P. Setny et al. “Solvent fluctuations in hydrophobic cavity-ligand binding kinetics”. In: *Proceedings of the National Academy of Sciences of the United States of America* 110.4 (2013), pp. 1197–1202. ISSN: 00278424 10916490.
- [65] R. Hausman et al. “Functionalization of polybenzimidazole membranes to impart negative charge and hydrophilicity”. In: *Journal of Membrane Science* 363.1-2 (2010), pp. 195–203. ISSN: 03767388.
- [66] M. Wanunu and A. Meller. “Chemically Modified Solid-State Nanopores”. In: *Nano Letters* 7.6 (2007). PMID: 17503868, pp. 1580–1585.
- [67] B. Yameen et al. “Single Conical Nanopores Displaying pH-Tunable Rectifying Characteristics. Manipulating Ionic Transport With Zwitterionic Polymer Brushes”. In: *Journal of the American Chemical Society* 131.6 (2009). PMID: 19159287, pp. 2070–2071.
- [68] J. Wagner and J. Keizer. “Effects of rapid buffers on Ca²⁺ diffusion and Ca²⁺ oscillations”. In: *Biophysical Journal* 67.1 (1994), pp. 447–456. ISSN: 0006-3495.
- [69] X. Lin et al. “Ultrathin Silica Membranes with Highly Ordered and Perpendicular Nanochannels for Precise and Fast Molecular Separation”. In: *ACS Nano* 9.11 (2015). PMID: 26458217, pp. 11266–11277.
- [70] Z. Sun et al. “Hierarchically Ordered Macro-/Mesoporous Silica Monolith: Tuning Macropore Entrance Size for Size-Selective Adsorption of Proteins”. In: *Chemistry of Materials* 23.8 (2011), pp. 2176–2184.
- [71] A. Calvo et al. “Mesoporous Films and Polymer Brushes Helping Each Other To Modulate Ionic Transport in Nanoconfined Environments. An Interesting Example of Synergism in Functional Hybrid Assemblies”. In: *Journal of the American Chemical Society* 131.31 (2009). PMID: 19722668, pp. 10866–10868.
- [72] M. B. Andersen et al. “Surface-dependent chemical equilibrium constants and capacitances for bare and 3-cyanopropyldimethylchlorosilane coated silica nanochannels”. In: *Journal of Colloid and Interface Science* 353.1 (2011), pp. 301–310. ISSN: 0021-9797.
- [73] V. Vitagliano and P. A. Lyons. “Diffusion Coefficients for Aqueous Solutions of Sodium Chloride and Barium Chloride”. In: *Journal of the American Chemical Society* 78.8 (1956), pp. 1549–1552.

S Supplement

Table S1: Basic parameters used in the PNP simulation

Parameters[units]	Value	Description
ϵ_o [F m ⁻¹]	8.854187×10^{-12}	Vacuum Permittivity
ϵ_r	78.5	Relative Permittivity
F [C mol ⁻¹]	96485	Faraday constant
T [K]	298	Temperature
D_H [m ² s ⁻¹]	9.31×10^{-9}	Diffusion constant of H ⁺ ⁷²
D_{OH} [m ² s ⁻¹]	5.30×10^{-9}	Diffusion constant of OH ⁻ ⁷²
D_{CF} [m ² s ⁻¹]	4.14×10^{-10}	Diffusion constant of 5(6)-Carboxyfluorescein ⁴²
D_{Cl} [m ² s ⁻¹]	2.03×10^{-9}	Diffusion constant of Cl ⁻ ⁷²
D_{Ca} [m ² s ⁻¹]	1.10×10^{-9}	Diffusion constant of Ca ²⁺ ⁷³
D_K [m ² s ⁻¹]	1.96×10^{-9}	Diffusion constant of K ⁺ ⁷²
pK_a	7.0	Equilibrium constant of reaction 3 ⁷²
pK_b	1.9	Equilibrium constant of reaction 4 ⁷²
pK_m	6.5	Ca ²⁺ adsorption equilibrium constant (Eq. 19) ⁵
η_{Total} [mol m ⁻²]	1.33×10^{-5}	Total density of silica functional group ^{8,72}

S.1 Supplemental figures

Table S2: Average electric potentials calculated at the two ends of nanopore (see Eq. 21) in KCl conductance validation(2D-axisymmetric)

[KCl]	$V_a(V)$	$V_b(V)$	$V_a - V_b(V)$	$\frac{V_a - V_b}{\delta\phi}$
1×10^{-6} M	0.192929	-0.002049	0.194978	97.489%
1×10^{-5} M	0.194460	0.000472	0.193988	96.994%
1×10^{-4} M	0.196105	0.002011	0.194094	97.047%
1×10^{-3} M	0.197282	0.001943	0.195339	97.670%
1×10^{-2} M	0.198244	0.001437	0.196807	98.404%
1×10^{-1} M	0.198898	0.001008	0.19789	98.945%

Table S3: Flux densities and ionic conductance corresponds to Fig. S5. Setting $[KCl] = 1\text{mM}$ and 10mM results in $\kappa D = 1.06$ and 3.35 , respectively ($D = 10.2\text{nm}$ is the diameter of nanopore). In Table S3 we show that increasing negative wall charge increases K^+ flux by about 60%, decreases Cl^- by 50%, leading to an overall increase in conductance of 50%. Further, increasing ionic strength supports a 10-fold increase in K^+ , 10 fold increase in Cl^- , and 5 fold increase in conductance overall.

Electric Potential (mV)	κD	Flux density ($\text{mol}/\text{m}^2 \cdot \text{s}$)				Conductance(S)
		J_K	J_{Cl}	J_H	J_{OH}	
$\phi = -10$	1.06	-0.258	0.034	-0.013	8.77×10^{-8}	2.028×10^{-10}
	3.35	-2.024	0.44	-0.0096	1.17×10^{-7}	1.053×10^{-9}
$\phi = -30$	1.06	-0.398	0.0177	-0.0189	4.57×10^{-8}	2.978×10^{-10}
	3.35	-2.83	0.29	-0.0134	7.57×10^{-8}	1.392×10^{-9}

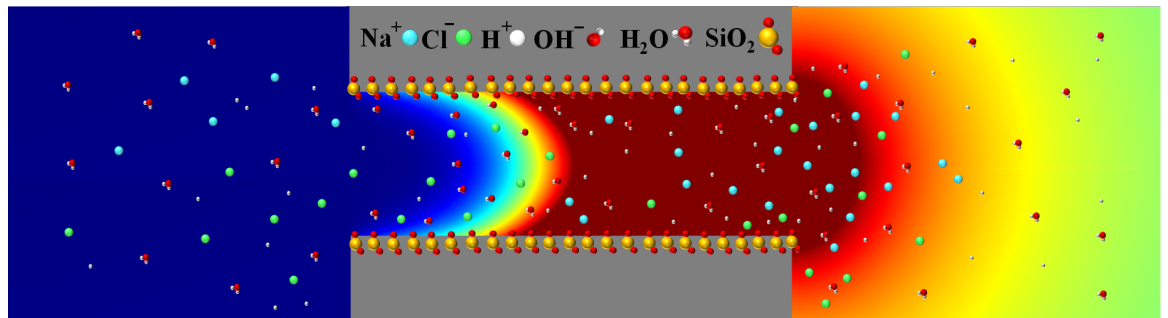


Figure S1: Schematic illustration of the ion transport in a two dimensional nanoslit system under consideration where a charge-regulated silica in a general salt solution containing multiple ionic species H^+ , OH^- , Na^+ , Cl^- , H_2O , SiO_2 . Adsorption of the metal cations occurs..

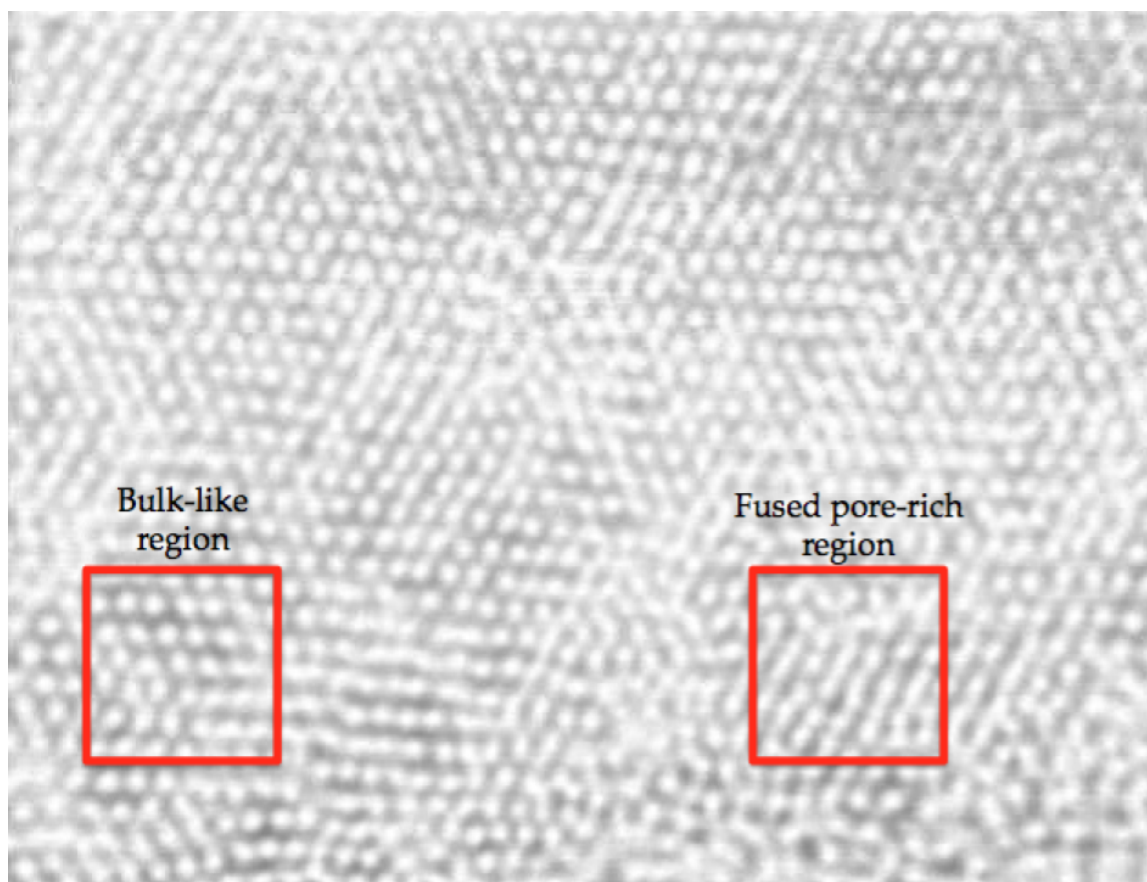


Figure S2: A representative TEM image of the 90nm-thick mesoporous silica film synthesized by Wooten et al.⁴² The data was collected at 68,000x magnification and span roughly 358nm by 450 nm. These data reveal a preponderance of ordered hexagonally-packed pore regions (bulk-like region) with a small number of defects evident as small linear features (fused pore-rich region).

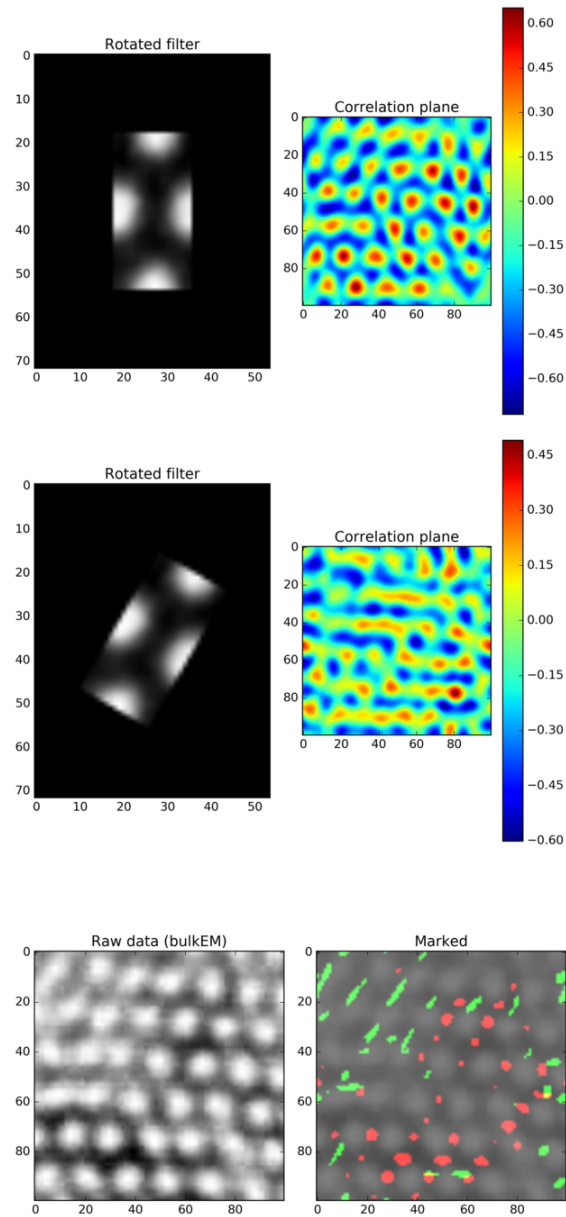


Figure S3: Matched filtering results for simulated transmission electron microscopy (TEM) images of a mesoporous silica film from Wooten et al.⁴² First and second rows correspond to the filters and corresponding matched filtering result at 0 and 30 degree rotations. Bottom row provides the raw data and an image denoting match filter detected fused pore (green) and bulk unit cell (red) features. .

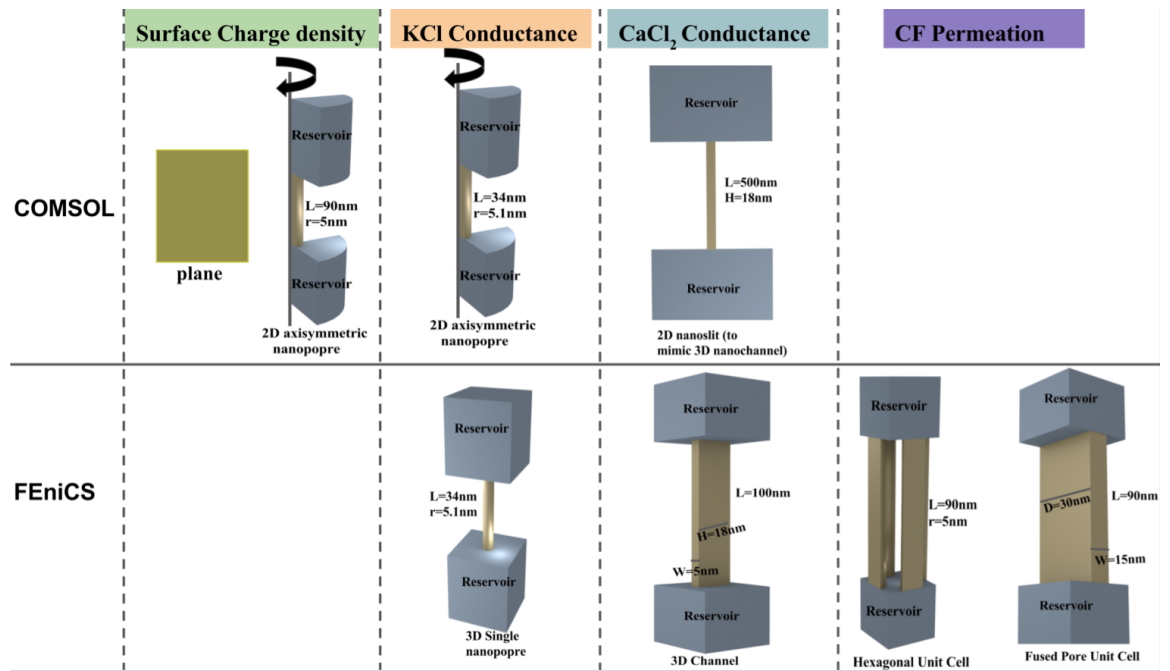


Figure S4: Illustration of all geometries used in simulations..

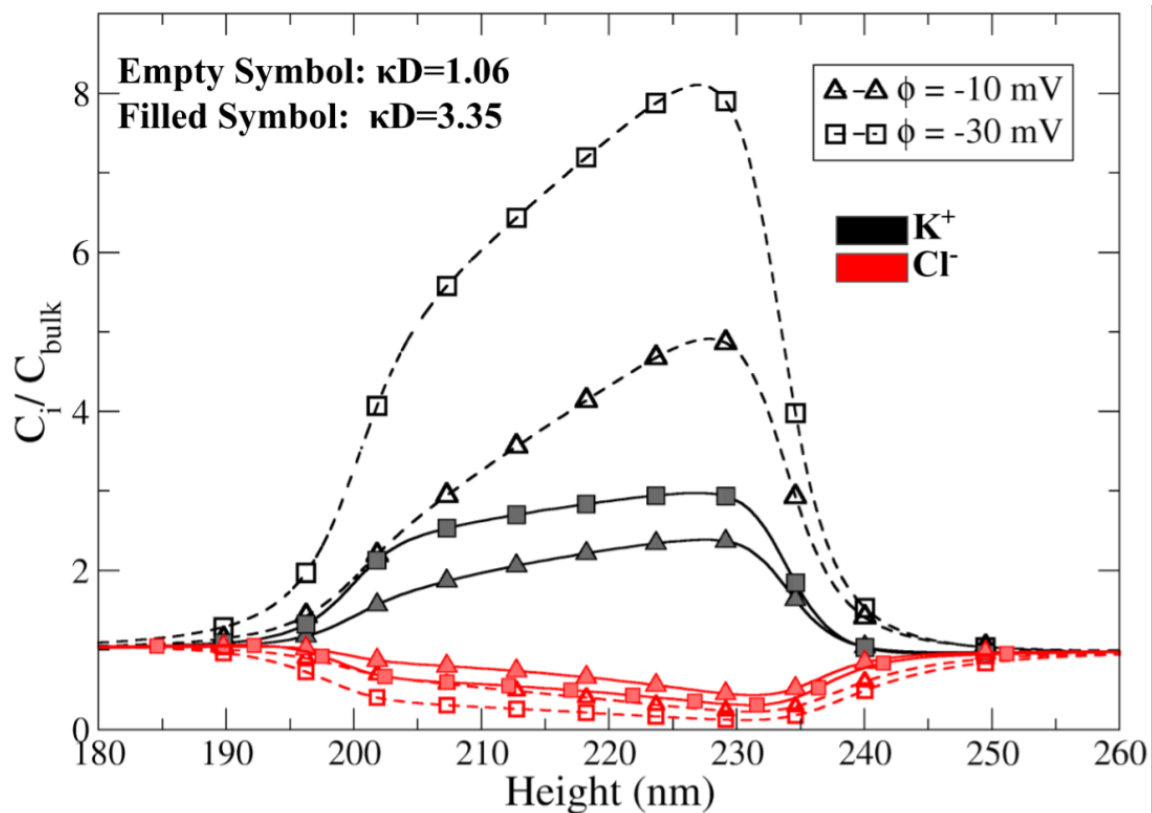


Figure S5: Concentration profile of K^+ and Cl^- along the center line of nanopore under different wall electric potentials and κD ($D=10.2 \text{ nm}$ is the diameter of nanopore). The height at x axis refers to the z direction: $0 < \text{height} < 200 \text{ nm}$ is bottom reservoir, $200 \text{ nm} < \text{height} < 234 \text{ nm}$ is nanopore and $234 \text{ nm} < \text{height} < 434 \text{ nm}$ is top reservoir. .

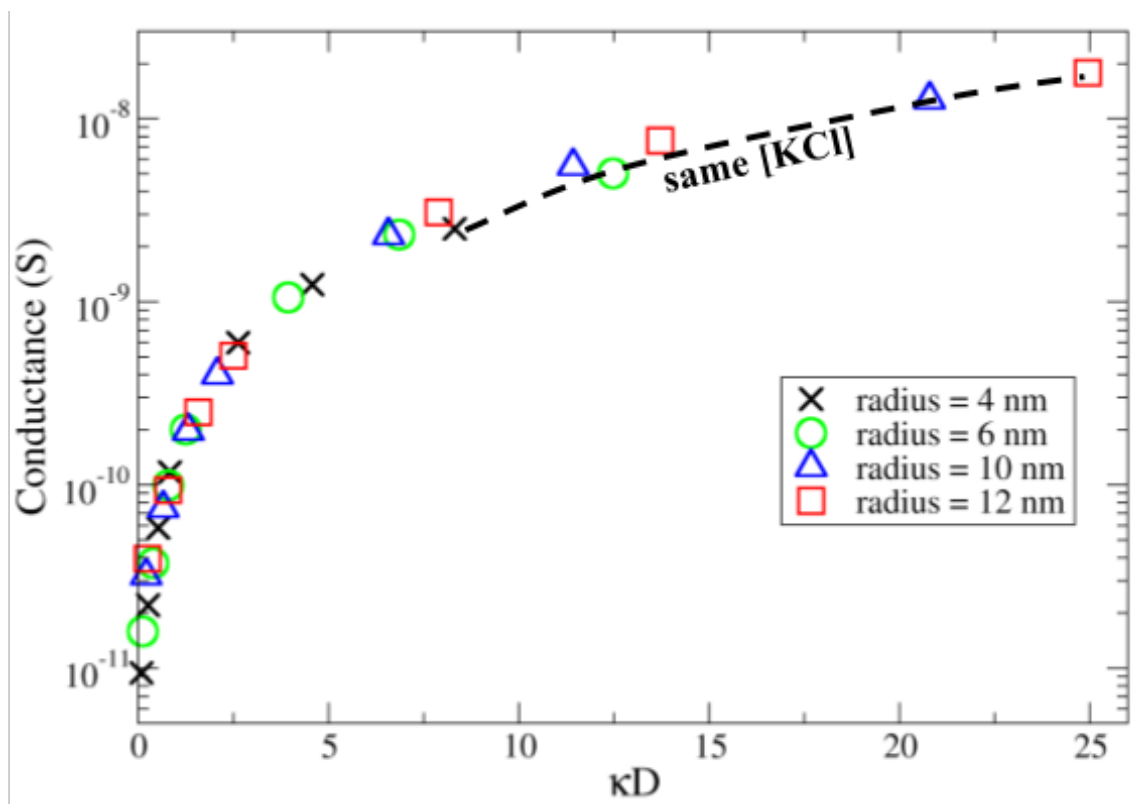


Figure S6: Numerical KCl conductance versus κD .

S.2 Supplemental results

S.2.1 Matched filter detection protocol and performance on real data

For the detection criterion in Eq. 7, we defined 'true positive' and 'false positive' metrics that we sought to maximize or minimize, respectively, for a given choice of $(\lambda_{\text{fused}}, \lambda_{\text{bulk}})$. These metrics were evaluated for two subsections of Fig. S2, a 'fused pore-rich' region and a 'bulk-like' region (see Methods). These regions were manually annotated with markers indicating the probable fused pore or bulk-like unit cells. The true positive metric was based on counting the number of above-threshold pixels for a given filter that overlapped with the hand-annotated markers. The false positive metric counted the number of above-threshold pixels that appeared anywhere in the complementary region, e.g. fused pore filter detections that occur in the bulk-like region and vice versa. Because the manual annotations were imprecise and the false positive pixels could scale with image size, we normalized the true positive and false positive rates by the pixel counts returned for the lowest threshold parameters considered. Hence, a minimal λ_{fused} value would return normalized true positive and false of 1.0, though the unnormalized values would typically be much larger for the true positive relative to false positive pixels. In Fig. S7 and Fig. S8, we present ROC curves to assess the relative true positives (correct detections) versus false positive (incorrect detections) as a function of a cutoff parameter, λ . Detections were evaluated via Eq. 7, for which detections above λ are designated as hits. In this study, we selected thresholds that minimized false positive rates, while still affording reasonably high true positive rates. For the fused pore unit cell, we selected $\lambda = 0.2$, while the $\lambda = 0.4$ was chosen for the bulk unit cell. These rates permitted roughly 60% true positive rates.

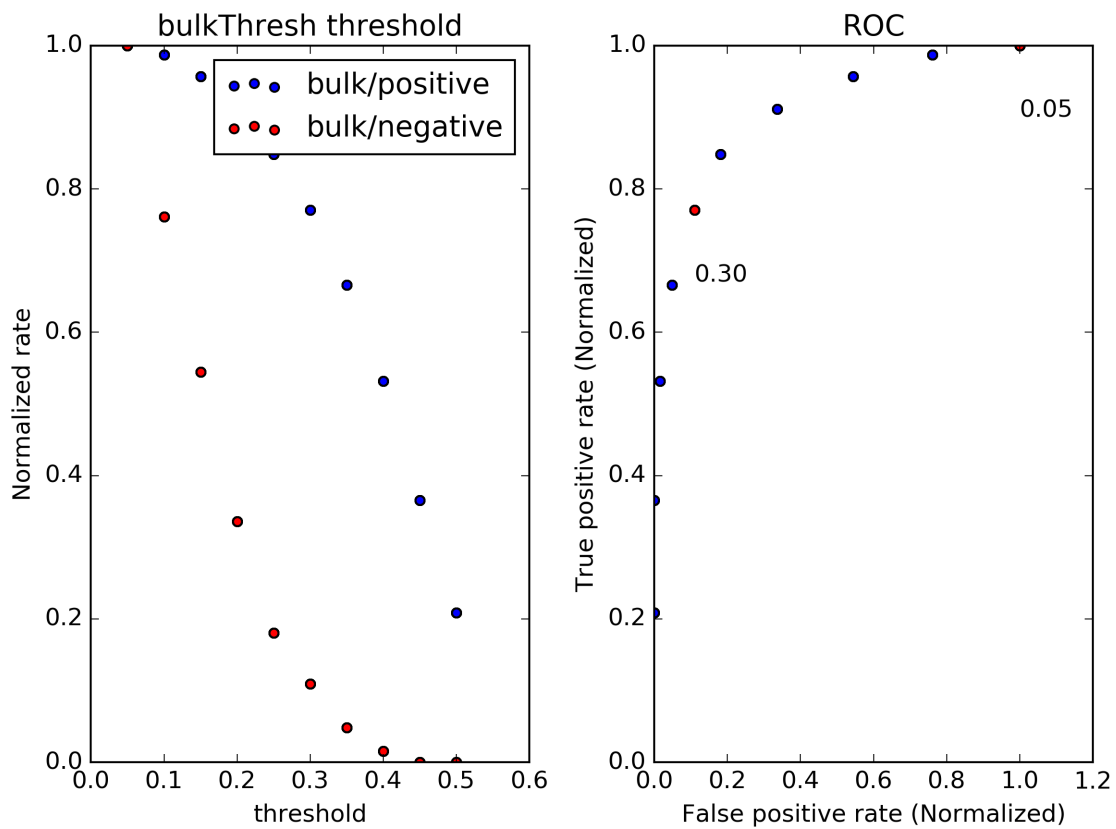


Figure S7: a) Normalize true positive (blue) and false positive (red) rates as a function of bulk filter threshold (λ). b) Corresponding receiver operator characteristic (ROC) curve. Thresholds are indicated in the plot. .

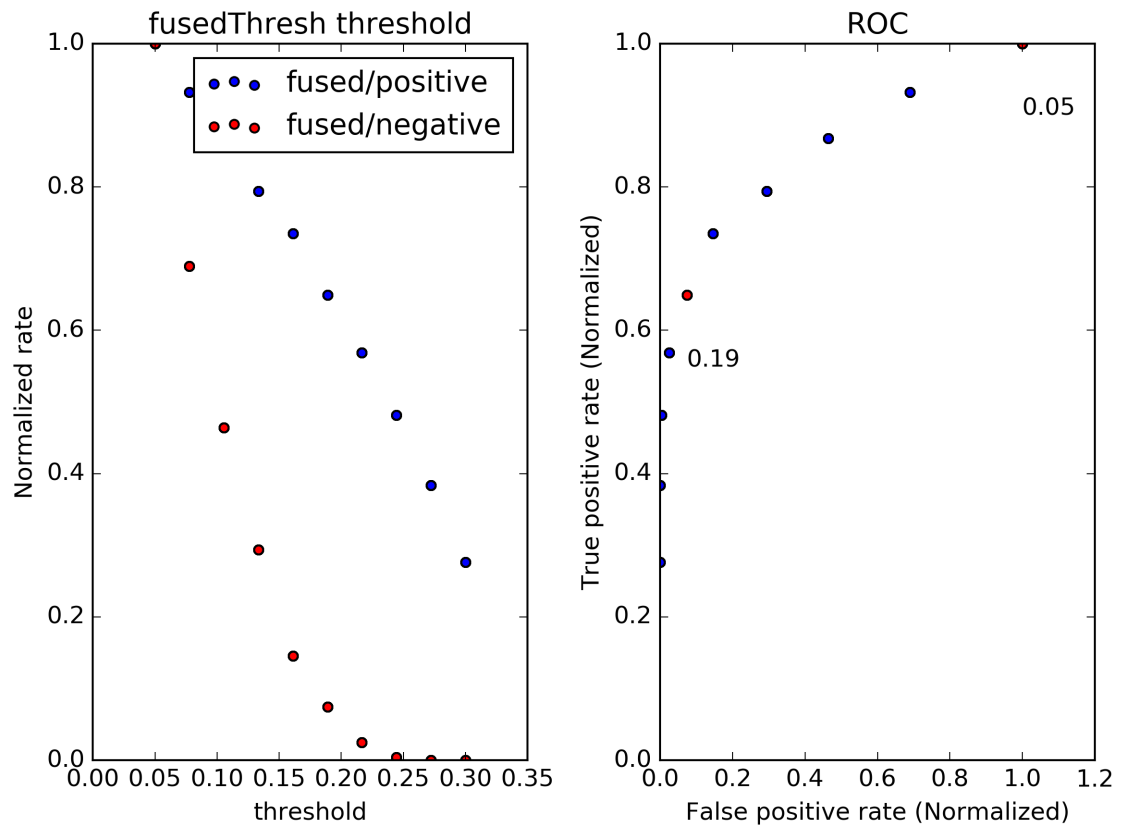


Figure S8: a) Normalize true positive (blue) and false positive (red) rates as a function of fused threshold (λ). b) Corresponding receiver operator characteristic (ROC) curve. Thresholds are indicated in the plot. .

S.2.2 Grahame equation for CaCl_2 salt solution

When the solution is composed of divalent cation (e.g., CaCl_2 solution), the Grahame equation used to relate wall electric potential (ϕ_0) and surface charge density (σ_s) is given as:

$$\sigma_s(\phi_0) = \sqrt{8\epsilon_o\epsilon_r k_B T} \sinh\left(\frac{e\phi_0}{2k_B T}\right) \left([CaCl_2](2 + \exp(\frac{-e\phi_0}{k_B T}))\right)^{0.5} \quad (\text{S1})$$

S.2.3 Validation of pH-regulated surface charge density

Main point: pH-effects can be well-approximated by simple model, allowing for more details 3D modeling. Potential empirical KH relationships

To test the ability of PNP model on describing silicate surface charge density, we numerically calculate the surface charge density of a planer silica film in contact with KCl aqueous solution. Silicate materials present a high density of hydroxyl groups, for which the ratio of Si-O^- to Si-OH_2^+ determines the surface charge density. Silanol groups are readily deprotonated/protonated thus the surface charge density can vary depending on the solution pH (see Eq. 12). Specifically, lower pH increases the extent of surface protonation, which thereby reduces the negative surface charge density. The surface charge density at the silicate materials is given by Eq. 19. For the purpose of validating our modeling results, we provide in Fig. S9 an analytical expression for σ_s at planar silica surface from Yeh et al:⁶¹

$$\sigma_s = \frac{2\epsilon_o\epsilon_r\kappa RT}{zF} \sinh\left(\frac{Fz\zeta}{2RT}\right) \quad (\text{S2})$$

$$\sigma_s = -F\Gamma_{total} \frac{K_a - K_b([H]_0 \exp(-\frac{F\zeta}{RT}))^2}{K_a + [H]_0 \exp(-\frac{F\zeta}{RT}) + K_b([H]_0 \exp(-\frac{F\zeta}{RT}))^2} \quad (\text{S3})$$

where κ is the inverse of Debye length, $[H]_0$ is the bulk proton concentration determined by pH, and ζ is zeta potential of the planar surface. After solving ζ through combination of Eq. S2 and Eq. S3, σ_s can be solved by substituting ζ into Eq. S3.

In Fig. S9 we present predictions of the surface charge density, σ_s for a planar silica film and a silica-based nanopore (length = 90 and radius = 5 nm, analogous to nanoporous film dimensions from⁴²) at several ionic strengths ($[\text{KCl}] \in [1, 1000]$ mM) and pH values (pH $\in [4, 8]$). These calculations were performed on 2D geometries (half-plane and axi-symmetric domain). Overall, the numerical results are in strong agreement with theoretical predictions. This is even the case for the nanopore, which is morphologically different from the planar domain assumed by the theoretical model. From these data, it is clear that increasing pH leads to a more negative surface charge density, which results from driving the silanol deprotonation reactions. At elevated ionic strengths, the models predict more negative deviations from the theoretical surface charge predictions. We attribute this trend to a greater degree of electrostatic shielding owing to the decreasing Debye length with increasing ionic strength, which reduces the favorability of attracting positively charged protons to the negatively charged surface. Another possible reason is due to the proton-cation competition mechanism:^{6,8} Protons will be more excluded from the hydroxyl groups due to high K^+ concentration, thus causing a more negative surface charge density. We also noticed that in Fig. S9B, σ_s of the nanopore scales with κD in a near-linear

manner. This linearity was confirmed by the high correlation coefficients of fitted lines, which is somewhat surprising, Yeh et al⁶ has shown that surface charge density near the pore mouth differs from that of the pore interior.

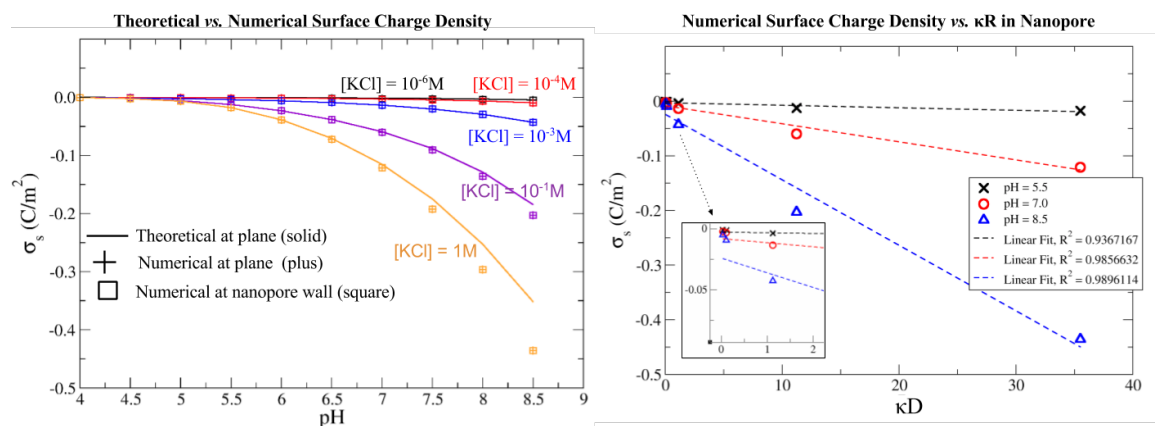


Figure S9: (A) Surface charge density, σ_s , for silica materials as a function of ionic strength ([KCl]) and pH. Numerical estimates are based on FEM simulations for a planar silica film (2D planar) as well as a 90 nm long pore with a 5 nm radius (2D axisymmetric), analogous to nanoporous film dimensions from⁴²). Validations are compared against a theoretical estimate (Eq. S2) for the surface charge of a planar silica film.⁶¹ (B) Surface charge density as a function of κD ($D = 10$ nm is the diameter) in the nanopore. .

S.3 KCl conductance using Navier-Stokes (fluid flow) and Poisson-Nernst-Planck formalisms

In Fig. S10 we present comparisons of experimental conductance data for a nanopore,⁷ including predictions using the PNP model augmented with fluid flow. For the PNP-Navier-Stokes model (PNPNS), the flux density of each ionic species is given by

$$J_i = -D_i \left(\nabla c_i + \frac{z_i F c_i}{RT} \nabla \phi \right) + \mathbf{u} c_i \quad (\text{S4})$$

where the last term denotes the contribution from convection and \mathbf{u} is the fluid velocity. The fluid velocity is solved subject to Navier-Stokes and continuity equations:

$$-\nabla p + \mu \nabla^2 \mathbf{u} = 0 \quad (\text{S5})$$

$$\nabla \cdot \mathbf{u} = 0 \quad (\text{S6})$$

where p and μ are the hydrodynamic pressure and the fluid viscosity, respectively. We set $p = 0$ and $\mu = 1 \times 10^{-3} \text{ Pa} \cdot \text{s}$ as that used in Yeh et al.⁶ Results from the PNP approach and PNPNS results are similar.

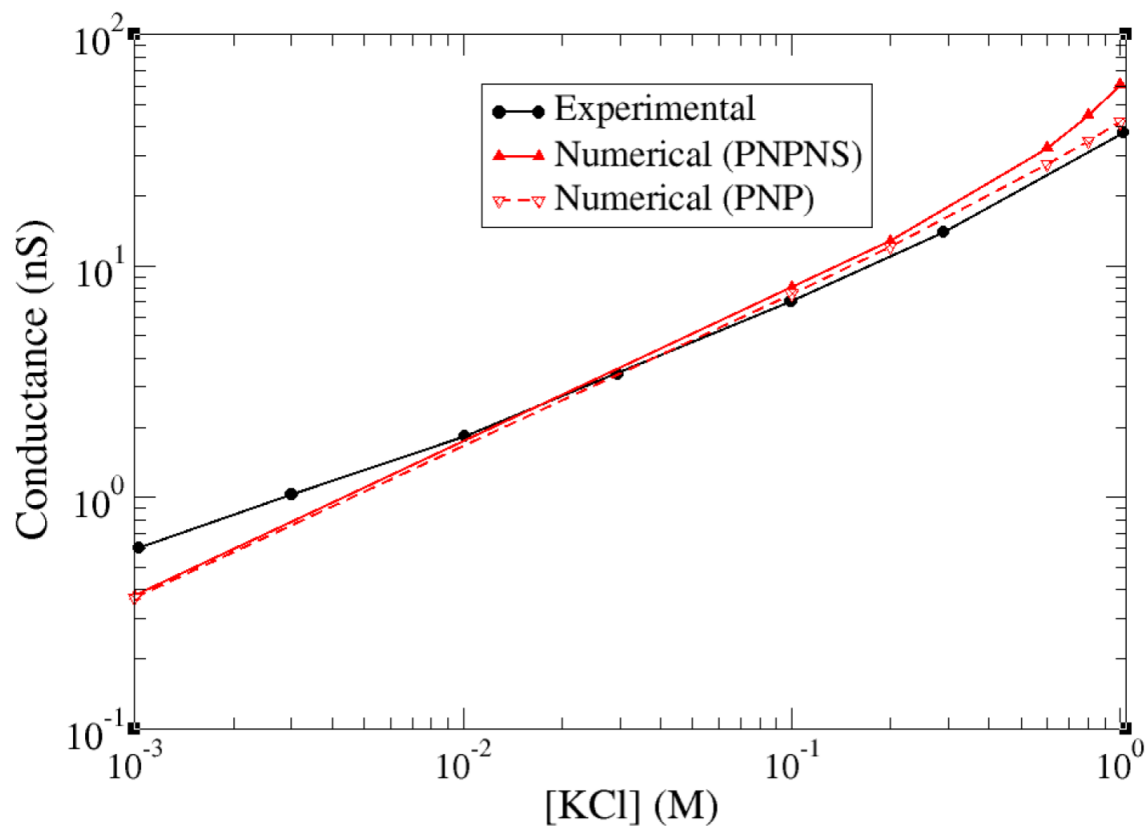


Figure S10: Experimental⁷ and predicted KCl conductance data in a nanopore, using Poisson-Nernst-Planck (PNP) theory and a PNP approach that includes fluid flow via Navier-Stokes equations. .

S.4 Ionic conductance of electrolyte solutions at varying wall electric potentials in nanopore/nanoslit

In order to investigate the sensitivity of the conductance results to our implementation of the charge-regulated silica surface, we predicted conductance of KCl and CaCl₂ at varying wall electric potentials (Fig. S11). For both KCl and CaCl₂, as the electric potential on the pore surface approaches 0, the conductance declines. While KCl is less sensitive to wall electric potential, CaCl₂ declines sharply as wall electric potential approaches 0. In addition, the sensitivity of conductance estimates to wall electric potential declines with increasing ionic strength, as the surface potential is shielded to a greater extent.

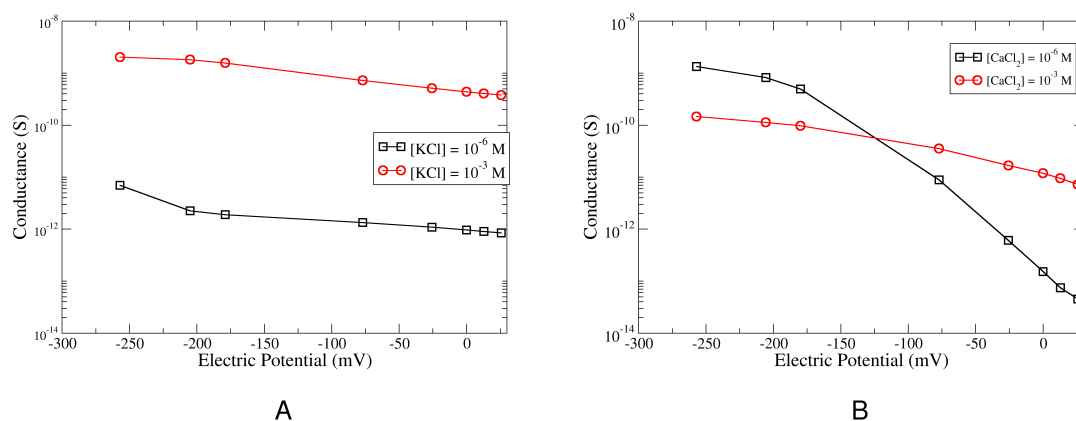


Figure S11: Ionic conductance at varying wall electric potentials. A) KCl ionic conductance(nanopore). B) CaCl₂ ionic conductance(nanoslit).

S.4.1 Characterization of Ca^{2+} adsorption at silica surface

The amount of Ca^{2+} adsorbed at the silica surface (n_{Ca}) was calculated as following: Assuming the layer formed by adsorbed Ca^{2+} is about 0.2nm thick ($l = 0.2\text{nm}$, comparable to the radius of Ca^{2+}). We do a volume integration of $[\text{Ca}]$ over this Ca^{2+} layer to get the total amount of absorbed Ca^{2+} . As shown in Fig. S12A: n_{Ca} increases linearly with the increasing of nanopore radius. This is because larger pore radii provides more surface onto which Ca^{2+} can be absorbed. In addition, n_{Ca} increases with the increasing of bulk $[\text{Ca}]$ at fixed radius. This is because higher $[\text{Ca}]$ will drive the Ca^{2+} adsorption reaction to the product end, resulting more Ca^{2+} being absorbed. We also characterized the percentage loss of Ca^{2+} (defined as $\frac{n_{Ca}}{N_{pore}}$, where N_{pore} is the total amount of Ca^{2+} in the nanopore). As shown in Fig. S12B: The largest percentage loss of Ca^{2+} due to absorption is about 30% to 35% when radius of nanopore is about 2nm and as radius increases, the percentage loss of Ca^{2+} decreases. This is because the volume of nanopore(denominator) expands more rapidly than that of Ca^{2+} layer. Also a larger bulk $[\text{Ca}]$ leads to a smaller percentage loss of Ca^{2+} since larger $[\text{Ca}]$ makes N_{pore} expand more rapidly, thus leading ratio of n_{Ca} to N_{pore} reduced.

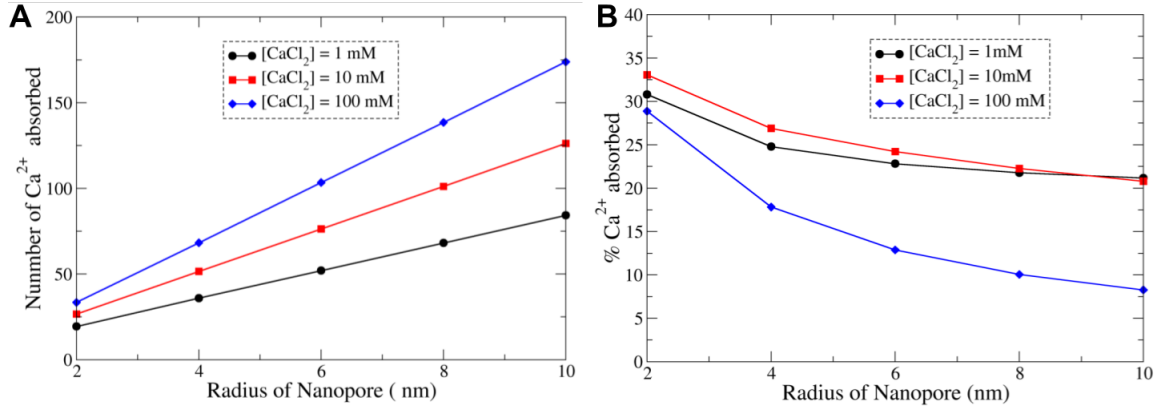


Figure S12: Amount of Ca^{2+} absorbed on the nanopore wall at pH=7 and with pore length = 90nm under varying nanopore radii(2D axisymmetric). A) The absolute amount of Ca^{2+} absorbed at silica surface. B) Percentage of Ca^{2+} absorbed(calculated as the bound Ca^{2+} divided by the total amount of Ca^{2+} in the nanopore).

S.4.2 Effects of porosity on permeability

Besides the electrostatic interaction, we also explored the packing compactness of nanopores on CF permeation. For clarity, we defined porosity as shown in Fig. S14 to characterize the packing compactness of nanopores on the silica membrane. While keeping nanopore radius $r = 5nm$ fixed, by changing the value of h and w , we can achieve hexagonal unit cells with different porosities. We then calculated CF permeability in these hexagonal cells at pH=7.4, bulk $[CF]=1mM$ and background ionic strength = 1mM. It can be shown clearly in Fig. S14 that, CF permeability linearly increases with porosity, indicating that a more compacted packing of nanopore will has higher CF permeability. Also at fixed porosity, a less negative electric potential permits a larger permeability, which is consistent with trends observed in Fig. 6.

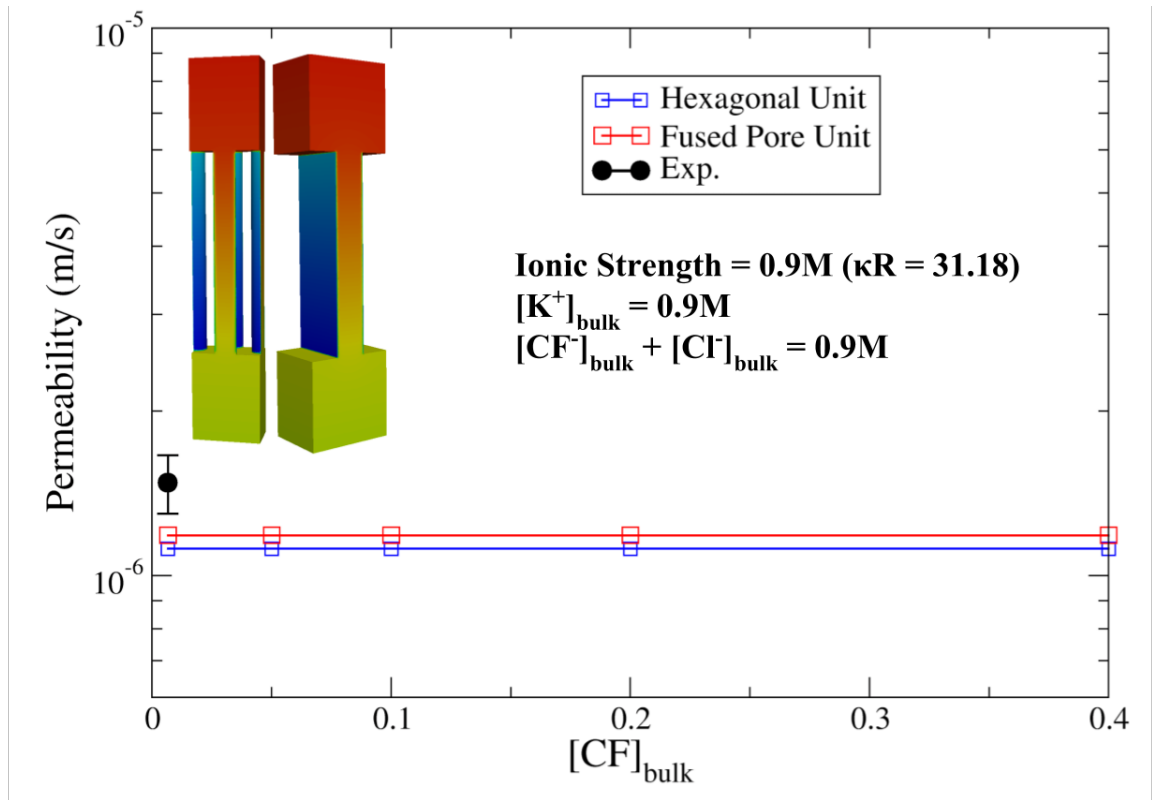


Figure S13: Numerically simulated permeability of CF passing through unit cell structures (dimensions are shown in Fig. 2). Total ionic strength is maintained as 0.9M which results $\kappa D = 31.18$ (κ is inverse of Debye length and $R = 10nm$ is diameter of nanopore). A fixed electric potential $\phi = -69.5mV$ (value is from a PNP+pH regulated surface charge model at pH = 7.4) was applied on the nanopore wall.

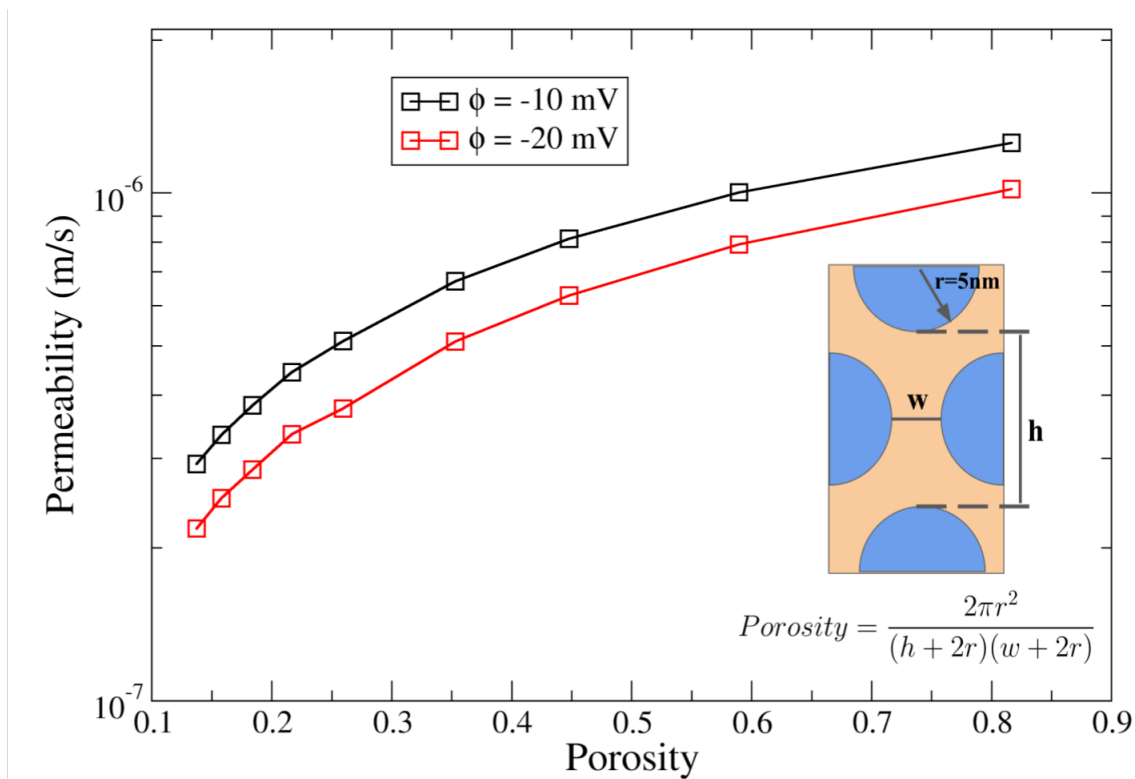


Figure S14: Permeability of CF vs. hexagonal unit cell porosity. Background ionic strength is set as 1mM and [CF] = 1mM. .